International Journal of Solids and Structures 257 (2022) 111264

Contents lists available at ScienceDirect

International Journal of Solids and Structures

journal homepage: www.elsevier.com/locate/ijsolstr

A new phenomenological constitutive model for shape memory alloys

Mohammed Y. Alsawalhi, Chad M. Landis *

Department of Aerospace Engineering and Engineering Mechanics and Oden Institute for Computational Engineering and Sciences, The University of Texas at Austin, Austin, TX, USA

ARTICLE INFO

Keywords:
Shape memory alloys
Constitutive modeling
Phase transformation

ABSTRACT

A new thermomechanical constitutive modeling approach for shape memory alloys (SMAs) that undergo a martensite to austenite phase transformation and the associated pseudoelastic and shape-memory responses is presented. The novelty of this new formulation is that a single transformation surface is implemented in order to capture the forward and reverse phase transformations, as well as the reorientation and detwinning of the martensite phase. The framework is akin to the usual flow theory plasticity with kinematic hardening, however in addition to the transformation strain there is also a transformation entropy that is directly related to the martensite volume fraction appearing in prior theories. A transformation surface in effective stress and effective temperature space is introduced and an associated flow rule governs the evolution of the transformation strain and entropy. In order to capture the multitude of SMA behaviors, a transformation potential function is introduced in transformation strain and entropy space for the derivation of the back stresses and back temperatures that define the kinematic hardening behavior. It is this potential function that governs all of the important behaviors within the model. After the description of the general theory, specific forms for the transformation surface and the transformation potential are devised and results for the behaviors captured by the model are provided for a range of thermomechanical loadings. Finally, the model is implemented in the finite element method and applied to the pseudoelastic and shape memory effects of a beam in pure bending.

1. Introduction

Shape memory alloys (SMAs) exhibit two unique properties, the shape memory effect and pseudoelasticity or superelasticity. The shape memory effect occurs when the material is cooled from a high temperature and then deformed. When the material is then heated back to a high temperature it recovers its original form. This behavior originates from the change in crystal structure from high temperature austenite, to twinned martensite upon cooling, to detwinned martensite when deformed, and then back to austenite when heated again. The amount of strain that can be recovered over such a thermomechanical excursion can approach 8% in some alloys. SMAs also exhibit pseudoelastic behavior, which is the ability of the material to recover large amounts of strain upon mechanical loading and unloading at temperatures above the martensite to austenite transition temperature. In this state, the thermodynamically favored austenite phase is driven to transform to detwinned martensite by the application of mechanical stress, Otsuka and Wayman (1999). Generally, the martensite phase consists of distinct regions each with different variants of the crystallographic directions of the single crystal, and the strain state of the material is dictated by the configuration of these variants. Macroscopically, twinned martensite will have nearly the same deformation state as the high temperature austenite that it transformed from. In twinned martensite, the variants appear in multiple orientations and form a self-accommodated ensemble. When loaded by an applied stress, unfavorably oriented martensite variants will transform to favorably oriented martensite variants via the mechanism of twin boundary motion to form detwinned martensite. Non-proportional loading of detwinned martensite can then cause subsequent twin boundary motion leading to a new set of crystallographic orientations of the martensite variants and an overall reorientation of the macroscopic strain, Lagoudas et al. (1996), Chatziathanasiou et al. (2016). Considering this range of behaviors, a useful phenomenological constitutive model for shape memory alloys must at least be able to capture each of these physical effects including the shape memory effect, pseudoelasticity, and martensite reorientation.

The thermomechanical behavior of SMAs has been studied at a range of length scales, Cisse et al. (2016). Continuum models have been used to study mechanisms like nucleation, twin growth, and phase interface motion, Abeyaratne and Knowles (1990), as well as the geometry of the phase and variant structures that form during transformation, Ball and James (1989), Bhattacharya et al. (2003). These

* Corresponding author.
E-mail address: landis@utexas.edu (C.M. Landis).

https://doi.org/10.1016/j.ijsolstr.2021.111264
Received 24 June 2021; Received in revised form 2 September 2021; Accepted 14 September 2021
Available online 29 September 2021

types of studies, along with phase-field simulations of phase and variant boundary motion Petryk et al. (2010), Petryk and Stupkiewicz (2010), Idesman et al. (2005), have contributed to a more complete understanding of SMA material behavior. However, the detailed analysis of the geometry and motion of every phase and variant boundary can be computationally intensive. At the next continuum scale, micro-mechanics models that utilize phase and variant volume fractions as internal variables have been constructed to study both single crystal and polycrystalline SMA behaviors, Aleong et al. (2002), Berveiller et al. (1991), Patoor and Berveiller (1997), Boyd and Lagoudas (1996), Patoor et al. (2006), Levitas and Stein (1997), Levitas and Ozsoy (2009). These types of micro-mechanical models contain several internal variables for each grain. The benefit of these micro-mechanical models resides in the relatively simple identification of the transformation systems between variants and the thermomechanical driving forces associated with each system. Polycrystalline SMA behavior is then simulated by modeling an aggregate of single crystals either by using self-consistent methods, or through direct computation on a simulated grain structure. These types of models can offer a great deal of insight into the transformations that occur at the single crystal level and how transformations in one grain can trigger or affect those in neighboring grains. However, this level of detail comes at a computational cost, and the implementation of these models in structural finite element calculations, where multiple grains would have to be simulated at each integration station in the model, is impractical. Thus, the need for phenomenological models with far fewer internal variables is motivated. Pioneering work on phenomenological models began with fundamental one-dimensional formulations, Tanaka (1986), Brinson (1993), Liang and Rogers (1997), Auricchio and Sacco (1997), and quickly progressed to include multiaxial response, Lagoudas et al. (1996), Qidwai and Lagoudas (2000a,b), Savi et al. (2002), Lagoudas et al. (2006), Popov and Lagoudas (2007), Ziolkowski (2007), Auricchio et al. (2009), Christ and Reese (2009), Arghavani et al. (2010), Hartl et al. (2010), Chemisky et al. (2011), Lagoudas et al. (2012), Sedlak et al. (2012), Frost et al. (2016), Scalet et al. (2019). These macroscopic phenomenological models focus on describing the evolution of macroscopic internal variables that describe the averaged phase and strain state of a polycrystal, which allows for a more efficient numerical implementation as compared to the micromechanical approaches based on the physics of the crystalline structural transformations, Lagoudas et al. (2006). One of the most pervasive internal variables that these models implement is the martensite volume fraction. This variable is then linked to the latent heat associated with the transformation from austenite to martensite. Additionally, the strain of the martensite is also introduced in a variety of ways, with some works making distinctions between twinned and detwinned martensite, Hartl et al. (2010), Chemisky et al. (2011), Lexcellent et al. (2006), Chatziathanasiou et al. (2016). Generally, these prior works have identified a set of transformation criteria, for forward phase changes from austenite to martensite, reverse phase changes from martensite to austenite, and for the reorientation of martensite Zhang and Baxevanis (2021). These transformation criteria are accompanied by flow rules governing the rates or increments of transformation, and with functional forms for how the transformation criteria change or "harden".

In contrast to these prior approaches, the ansatz for the model presented herein is that forward and reverse transformation, and martensite reorientation can all be captured with a single transformation criteria and an associated flow rule. The critical features of SMA behavior must be captured by a carefully crafted hardening potential which is used for the derivation of back stresses and temperatures that define the kinematic hardening laws within the model. This approach is similar to that previously established for the deformation of polycrystalline ferroelastic materials, which utilized a yield surface defined in an effective stress space and a hardening potential in terms of the remanent strain, Landis (2003). Landis utilized micromechanical models to inform the phenomenological framework with an effective remanent strain parameter that was able to account for the strain asymmetry in tension versus compression. A similar framework was applied by Jiang and Landis to the isothermal behavior of the pseudoelastic response in SMAs, and was also coupled with standard plasticity for very high stress loadings, Jiang and Landis (2016). Jiang and Landis (2016) also tackled the problem of tension/compression asymmetry in the stress levels required for the initiation of transformation through a weighted mixture of tension and compression potentials that are fitted to experimental stress–strain curves.

One interesting feature of SMA stress–strain behavior is the existence of asymmetry between tension and compression. Experimental measurements show that in compression the transformation strain is lower, the stress level is higher, and the slope of the stress–strain curve is steeper during transformation, Gall et al. (1999), Paiva et al. (2005). Several of the previous studies cited have also accounted for this asymmetry between tension and compression, Gillet et al. (1998), Raniecki and Lexcellent (1998), Qidwai and Lagoudas (2000b), Landis (2003), Peultier et al. (2008), Chemisky et al. (2011), Frost et al. (2016), Zhang and Baxevanis (2021).

The model to be presented here will extend this framework to non-isothermal behavior by including an additional internal variable, akin to the martensite volume fraction, which we call the transformation entropy to account for the possibility of thermally driven phase changes. Hence, the transformation strain tensor and the transformation entropy will serve as the internal variables for the model. Note that other models identify the martensite volume fraction f_M as an internal variable and the transformation entropy is directly related to f_M as $s^t = (1 - f_M)(s_A - s_M)$ where $(s_A - s_M)$ is the difference in entropy between the pure austenite and pure martensite phases. The elements of the present theory include a transformation surface in an effective temperature and stress space, an associated flow rule for the evolution of the transformation strain and transformation entropy, and finally a hardening potential that is dependent on the transformation strain and transformation entropy which governs the derivation of the back stress and back temperature.

2. Methodology

As described in the prior section, the transformation strain, ε^t_{ij}, and transformation entropy, s^t, are employed as internal variables in this theory. We postulate that the Helmholtz free energy of the material takes the form,

$$\begin{aligned}\Psi =& \frac{1}{2}c_{ijkl}\left(\varepsilon_{ij}-\varepsilon^t_{ij}\right)\left(\varepsilon_{kl}-\varepsilon^t_{kl}\right)-\beta_{ij}\left(\varepsilon_{ij}-\varepsilon^t_{ij}\right)\theta \\ &+ C\left(\theta-\theta_0-\theta\ln\frac{\theta}{\theta_0}\right)-\theta s^t \\ &+ \Psi^t(\varepsilon^t_{ij},s^t)\end{aligned} \tag{1}$$

where the first three terms are the reversible energy that depend on the total strain ε_{ij}, transformation strain, and temperature θ. The material properties include the elastic moduli, c_{ijkl}, thermal expansion moduli, β_{ij}, and the specific heat capacity, C. The last two terms include the transformation entropy contribution to the free energy and the hardening potential Ψ^t, which depends only on the transformation strain and transformation entropy.

The pointwise form of the second law of thermodynamics can be written as,

$$\dot{\Psi} \leq \sigma_{ij}\dot{\varepsilon}_{ij} - s\dot{\theta} - \frac{1}{\theta}q_i\theta_{,i} \tag{2}$$

where q_i is the heat flux, $\theta_{,i}$ is the temperature gradient, and the stress, σ_{ij}, and total entropy, s, are derived from the Helmholtz free energy as,

$$\sigma_{ij} = \frac{\partial\Psi}{\partial\varepsilon_{ij}} = c_{ijkl}(\varepsilon_{kl}-\varepsilon^t_{kl}) - \beta_{ij}\theta \tag{3}$$

$$s = -\frac{\partial\Psi}{\partial\theta} = \beta_{ij}\left(\varepsilon_{ij}-\varepsilon^t_{ij}\right) + C\ln\frac{\theta}{\theta_0} + s^t \tag{4}$$

The second law then becomes,

$$\underbrace{\left(\sigma_{ij}-\sigma_{ij}^{B}+\bar{\sigma}_{ij}\right)}_{\hat{\sigma}_{ij}}\dot{\varepsilon}_{ij}^{t}+\underbrace{\left(\theta-\theta^{B}+\bar{\theta}\right)}_{\hat{\theta}}\dot{s}^{t}-\frac{1}{\theta}q_i\theta_{,i}\geq 0 \tag{5}$$

Here, the back stress, σ_{ij}^{B}, and the back temperature, θ^{B}, are given as,

$$\sigma_{ij}^{B}=\frac{\partial\Psi^{t}}{\partial\varepsilon_{ij}^{t}} \tag{6}$$

$$\theta^{B}=\frac{\partial\Psi^{t}}{\partial s^{t}} \tag{7}$$

Additionally, the stress-like and temperature-like terms, $\bar{\sigma}_{ij}$ and $\bar{\theta}$, account for the possibility that the reversible properties of the material depend on the internal variables. For the assumed form of the free energy given in Eq. (1) these terms are,

$$\begin{aligned}\bar{\sigma}_{ij}=&\frac{1}{2}\frac{\partial c^{-1}_{pqrs}}{\partial\varepsilon_{ij}^{t}}\sigma_{pq}\sigma_{rs}+\frac{\partial\alpha_{pq}}{\partial\varepsilon_{ij}^{t}}\sigma_{pq}\theta\\&+\frac{1}{2}\frac{\partial\bar{C}}{\partial\varepsilon_{ij}^{t}}\theta^{2}+\frac{\partial C}{\partial\varepsilon_{ij}^{t}}\left(\theta-\theta_0-\theta\ln\frac{\theta}{\theta_0}\right)\end{aligned} \tag{8}$$

$$\begin{aligned}\bar{\theta}=&\frac{1}{2}\frac{\partial c^{-1}_{pqrs}}{\partial s^{t}}\sigma_{pq}\sigma_{rs}+\frac{\partial\alpha_{pq}}{\partial s^{t}}\sigma_{pq}\theta\\&+\frac{1}{2}\frac{\partial\bar{C}}{\partial s^{t}}\theta^{2}+\frac{\partial C}{\partial s^{t}}\left(\theta-\theta_0-\theta\ln\frac{\theta}{\theta_0}\right)\end{aligned} \tag{9}$$

where $\alpha_{ij}=c^{-1}_{ijkl}\beta_{kl}$ is the thermal expansion tensor, and $\bar{C}=\alpha_{ij}\beta_{ij}$ is a contribution to the specific heat at constant pressure. Eq. (5) also defines the thermodynamic driving forces $\hat{\sigma}_{ij}$ for the transformation strain and $\hat{\theta}$ for the transformation entropy.

At this juncture, we do not attempt to satisfy this inequality in a completely general way, but instead take a "strong form" approach where we assume that the first two terms satisfy the inequality independently of the third heat conduction term. This can be accomplished by taking the heat flux to satisfy,

$$q_i=-k_{ij}\theta_{,i} \tag{10}$$

and then taking the increments of transformation strain and transformation entropy to abide by the following flow rule,

$$\dot{\varepsilon}_{ij}^{t}=\lambda\frac{\partial\Phi}{\partial\hat{\sigma}_{ij}} \tag{11}$$

$$\dot{s}^{t}=\lambda\frac{\partial\Phi}{\partial\hat{\theta}} \tag{12}$$

$$\Phi(\hat{\sigma}_{ij},\hat{\theta},\varepsilon_{ij}^{t},s^{t})=0 \tag{13}$$

where λ is a positive multiplier, and Φ is a transformation surface that encloses the origin in the driving force space, and is convex. The convexity of the transformation surface also ensures that the postulate of maximum plastic dissipation is satisfied.

It is possible to manipulate Eqs. (3), (4), (8), (9), (11), (12), and (13) to obtain either continuum tangent moduli, or numerical integration schemes relating increments of stress and entropy to increments of strain and temperature. Such a numerical scheme for finite element calculations is detailed in the Appendix. However, the important challenge for the material model is to specify the hardening potential Ψ^{t} and the transformation surface Φ in a manner that captures the material behaviors exhibited by SMAs. That challenge is addressed in the following section.

3. Material modeling

Following Jiang and Landis (2016) the transformation surface is taken to be spherical in deviatoric effective stress space, and is extended to the effective temperature space as follows.

$$\Phi=\frac{3}{2}\frac{\hat{s}_{ij}\hat{s}_{ij}}{\sigma_0^{2}}+\frac{\hat{\theta}^{2}}{\theta_0^{2}}-1 \tag{14}$$

where $\hat{s}_{ij}$ is the deviatoric effective stress, σ_o and θ_o are, respectively, the normalizing stress temperature respectively. These two parameters set the width of the hysteresis in the stress–strain and temperature–entropy behaviors of the material. Note, that the assumption that the transformation surface depends only on the deviatoric stress implies that the transformation strain is volume conserving, and as such this form is neglecting any differences in volume between the austenite and martensite phases of the material. Such enhancements are of course possible, but are not included in the present material description. We point out that the magnitude of σ_0 is significantly smaller than the apparent transformation stress from austenite to martensite at high temperatures, i.e. the stress level where significant amounts of transformation occur, and so it is the formulation of the hardening potential that leads to such transformation stresses and the dependence of these stresses on the temperature.

As assumed in Eq. (1), the transformation potential will depend only on the internal variables ε_{ij}^{t} and s^{t}. In addition to the temperature dependence of the transformation stress behaviors, it must also be formulated to capture the tension/compression asymmetry in the strain saturation behavior and in the hardening behaviors in tension versus compression. The functional form of the overall transformation potential that we propose is,

$$\Psi^{t}=\xi\Psi_{C}^{t}(J_2^{t},\bar{\varepsilon},s^{t})+(1-\xi)\Psi_{T}^{t}(J_2^{t},\bar{\varepsilon},s^{t})+\Psi_{s}(s^{t}) \tag{15}$$

Here Ψ_{T}^{t} and Ψ_{C}^{t} are potentials for the tensile and compressive responses of the material, and ξ is a function of the internal variables that interpolates between them with $\xi=0$ for uniaxial extension and $\xi=1$ for uniaxial compression. All other values of ξ between 0 and 1 represent other transformation strain states. The $\bar{\varepsilon}$ variable takes the tensorial transformation strain and accounts for the tension/compression asymmetry in strain with a scalar variable. Its description is provided in more detail below.

Both ξ and $\bar{\varepsilon}$ are dependent on the invariants of the deviatoric transformation strain J_2^{t} and J_3^{t}. Where,

$$J_2^{t}=\left(\frac{2}{3}e_{ij}^{t}e_{ij}^{t}\right)^{\frac{1}{2}} \tag{16}$$

$$J_3^{t}=\left(\frac{4}{3}e_{ij}^{t}e_{jk}^{t}e_{ki}^{t}\right)^{\frac{1}{3}} \tag{17}$$

Since it is prevalent in our formulation, we also define the ratio of these invariants,

$$J_r=\frac{J_3^{t}}{J_2^{t}} \tag{18}$$

ξ and $\bar{\varepsilon}$ are then defined as

$$\bar{\varepsilon}=J_2^{t}f(J_r) \tag{19}$$

$$\xi(J_r)=\frac{1-J_r^{3}}{2} \tag{20}$$

The function f, originally proposed by Landis (2002, 2003) and then modified by Jiang and Landis (2016), is a function of J_r that is responsible for the strain asymmetry between tension and compression. Certain conditions must be met when choosing f as described in Landis (2003). Specifically the first, second, fourth and fifth derivatives must be equal zero at $J_r=0$, i.e. $f^{I}(0)$, $f^{II}(0)$, $f^{IV}(0)$, and $f^{V}(0)=0$. Similarly if choosing a different form for $\xi(J_r)$ than the simple prescription in Eq. (20), then $\xi^{I}(0)$, $\xi^{II}(0)$, $\xi^{IV}(0)$, and $\xi^{V}(0)=0$, Jiang and Landis (2016). Landis (2003) showed how the function f can be determined from micromechanics calculations, however simple functions can instead be selected to fit the behaviors in tension, compression, and pure shear that along with the constraints on the derivative of f at $J_r=0$ perform well within the theory. One such functional form proposed by Sedlak et al. (2012) and also used by Jiang and Landis (2016) is,

$$f=\cos\left[\frac{\cos^{-1}\left[1-a(J_r^{3}+1)\right]}{3}\right] \tag{21}$$

Given $\xi(J_r)$ and $f(J_r)$, one can derive σ^B_{ij} and θ^B as

$$\begin{aligned}\sigma^B_{ij} &= \frac{d\Psi^t}{d\varepsilon^t_{ij}} \\ &= \xi\left(\frac{\partial\Psi^t_C}{\partial\bar{\varepsilon}}\frac{d\bar{\varepsilon}}{d\varepsilon^t_{ij}} + \frac{\partial\Psi^t_C}{\partial J^t_2}\frac{dJ^t_2}{d\varepsilon^t_{ij}}\right) \\ &+ (1-\xi)\left(\frac{\partial\Psi^t_T}{\partial\bar{\varepsilon}}\frac{d\bar{\varepsilon}}{d\varepsilon^t_{ij}} + \frac{\partial\Psi^t_T}{\partial J^t_2}\frac{dJ^t_2}{d\varepsilon^t_{ij}}\right) \\ &+ \xi'\frac{\partial J_r}{\partial\varepsilon^t_{ij}}\left(\Psi^t_C - \Psi^t_T\right) \end{aligned} \tag{22}$$

$$\theta^B = \frac{\partial\Psi^t}{\partial s^t} = \xi\frac{\partial\Psi^t_C}{\partial s^t} + (1-\xi)\frac{\partial\Psi^t_T}{\partial s^t} + \frac{\partial\Psi_s}{\partial s^t} \tag{23}$$

Under uniaxial tension or compression Eqs. (22), (23) can be reduced while noting that the last term in Eq. (22) goes to zero due to $\frac{dJ_r}{d\varepsilon^t_{11}} = 0$ for uniaxial strain states, Jiang and Landis (2016).

$$\sigma^B_{11c} = \frac{\partial\Psi^t_C}{\partial\bar{\varepsilon}}\frac{d\bar{\varepsilon}}{d\varepsilon^t_{11}} + \frac{\partial\Psi^t_C}{\partial J^t_2}\frac{dJ^t_2}{d\varepsilon^t_{11}} \tag{24}$$

$$\sigma^B_{11t} = \frac{\partial\Psi^t_T}{\partial\bar{\varepsilon}}\frac{d\bar{\varepsilon}}{d\varepsilon^t_{11}} + \frac{\partial\Psi^t_T}{\partial J^t_2}\frac{dJ^t_2}{d\varepsilon^t_{11}} \tag{25}$$

$$\theta^B_c = \frac{\partial\Psi^t_C}{\partial s^t} + \frac{\partial\Psi_s}{\partial s^t} \tag{26}$$

$$\theta^B_t = \frac{\partial\Psi^t_T}{\partial s^t} + \frac{\partial\Psi_s}{\partial s^t} \tag{27}$$

Notice that even under the assumption that $\Psi^t_C = \Psi^t_T$, Eqs. (24) and (25) indicate that there will still be asymmetry between tension and compression due to the asymmetry in the $\frac{d\bar{\varepsilon}}{d\varepsilon^t_{11}}$ term.

4. Formulation of the hardening potentials

4.1. Physical considerations for the model

The present approach differs from others in that the size of the transformation surface, as characterized by σ_0 and θ_0, does not in general dictate the level where transformation occurs, especially at high temperature. Instead, σ_0 and θ_0 dictate the size of the hysteresis loops in the mechanical and thermal behavior. This feature of the model is what allows it to capture forward phase transformation from austenite to martensite, reverse phase transformation from martensite to austenite, and martensite reorientation all with a single transformation surface and associated flow rule. As mentioned previously, the transformation surface Φ cannot be used to capture the very large transformation stresses in SMAs that arise at high temperatures. Instead, this feature of the material behavior is captured by the suitable construction of the hardening potential Ψ^t that governs the kinematic hardening response within the model. Specifically, to model the high transformation stresses observed at high temperature, the hardening that occurs upon the initial intersection of the loading with the transformation surface must be so large as to mimic elastic response until a stress level where significant transformation strains can accumulate is achieved.

A second feature of SMA material behavior that must be encoded within the hardening potentials is the recognition that the maximum amount of transformation strain that can develop in the transformation from austenite to martensite is finite. Similarly, the amount of latent heat expelled during the transformation, which is governed by the transformation entropy, is also finite. Contrast such behavior to the essentially unlimited amount of plastic strain that can accrue in metals. Both the high stress hardening that occurs at high temperature and the constraint of finite transformation strain, ε^t_{ij}, and entropy, s^t, are achieved by mapping out the domain of possible transformation states in transformation strain and entropy space and selecting hardening functions that prohibit states outside of this domain. First, recognize that the strain-like variable $\bar{\varepsilon}$ defined in Eq. (19) maps all possible deviatoric transformation strain states onto a uniaxial compression. Hence, defining ε_0 as the amount of compressive strain that can be achieved by polycrystalline martensite, one constraint on the transformation state domain is that the transformation strain characterized by $\bar{\varepsilon}$ and adjusted for the volume fraction of martensite must be less than ε_0. Furthermore, the transformation entropy can readily be used as a measure of the martensite volume fraction by noting that the transformation entropy can evolve from a minimum of zero when the material is 100% martensite to a maximum of s_0 when the material is 100% austenite. Therefore the proposal in this work is to introduce an asymptote in the strain-entropy coupled part of hardening potential as $\left(1 - \bar{\varepsilon}/\varepsilon_0 - s^t/s_0\right)$ goes to zero. A second part of the hardening potential that only depends on the transformation entropy is also required to allow for stress-free phase transformation.

A schematic representation of the strain-entropy coupled part of the hardening potential is illustrated in Fig. 1. To illustrate how this leads to behaviors observed in SMAs first consider the case of twinned martensite at low temperature. In this state the transformation strain and the transformation entropy will each be zero. Now consider the application of stress to the material in this state under isothermal low temperature conditions. Notice that at low levels of transformation strain the slope of the hardening potential with respect to the strain direction is small, which translates to a small back stress which implies that the transformation stress for the material at low temperature is σ_0. As the transformation strain approaches ε_0 the slope of the potential increases without bound which means that the back stress also increases and the applied stress along with it. Since there is an asymptote as $\bar{\varepsilon} \to \varepsilon_0$ the transformation strain cannot increase beyond this limit and the applied stress will continue to grow elastically as more strain is applied. The process described is the detwinning of martensite that occurs when stress is applied to twinned martensite at low temperature. If the applied stress is removed at this state the back stress does have to decrease from its previously high levels, but due to the asymptote it does so at very small changes in the transformation strain. The complete removal of the applied stress will result in a persistent strained/detwinned martensite state. If an increase in temperature is now applied to the material at zero stress, the transformation entropy will be driven towards s_0. However, due to the constraints of what can be described as the "asymptotic wall", increases in transformation entropy must be accompanied by decreases in the transformation strain, which will approach zero as $s^t \to s_0$. Physically, this behavior is the shape memory effect where detwinned martensite is transformed back to austenite. Next consider the behavior at high temperatures where the transformation entropy is close to s_0 in the stress-free state. In this situation the domain defined by $0 < \left(1 - \bar{\varepsilon}/\varepsilon_0 - s^t/s_0\right) < 1$ requires that the transformation strain is essentially zero, which it should be since the stress-free high temperature phase is austenite. Notice that in this state the slope of the hardening potential is high with respect to both the strain and entropy directions. The state resides on the previously named asymptotic wall. Note also that at such points not only is the back stress high, but changes in the back stress with respect to changes in strain are also high. This feature leads to nearly linear elastic behavior, i.e. very large changes in back stress for very small changes in transformation strain. It is also important to recognize that as stress is applied to the material, transformation strain cannot accumulate unless the transformation entropy decreases. Physically this is the stress induced austenite to martensite transformation that occurs during pseudoelastic behavior. Such increases in transformation strain and decreases in transformation entropy occur as the state moves along the asymptotic wall towards the corner of the transformation domain at $\bar{\varepsilon} = \varepsilon_0$ and $s^t = 0$. Furthermore, notice that higher temperatures push the path of the transformation state higher up on the asymptotic wall since temperature drives the entropy to increase. This then requires higher states of applied stress to drive the increases in transformation strain and pull the transformation entropy lower. If the stress is then removed, the driving force of the

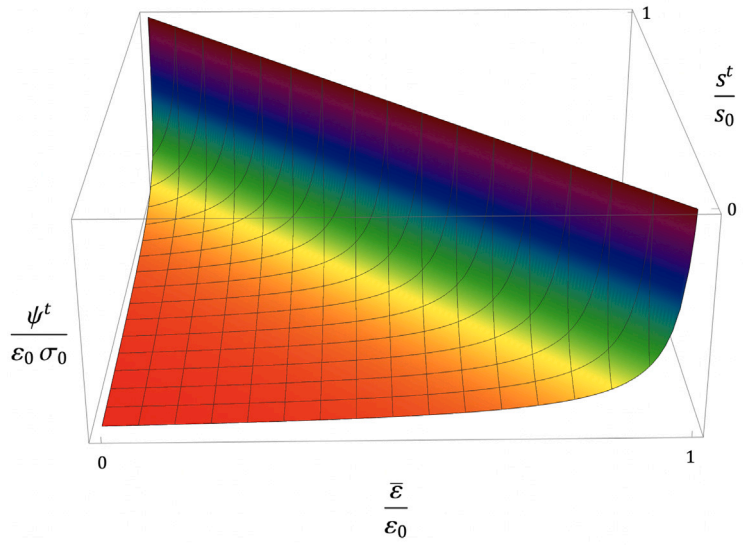

Fig. 1. A schematic of the strain-entropy coupled part of the hardening potential.

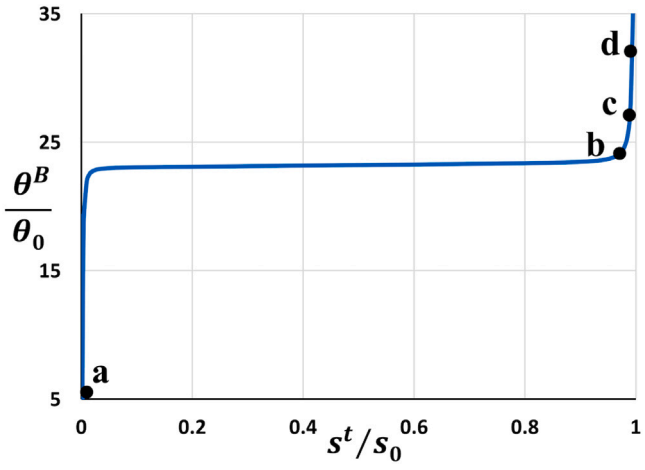

Fig. 2. The back temperature versus the transformation entropy derived from Eq. (30) for the material parameters given in Table 1. The points (a)–(d) correspond to temperatures where the stress–strain behavior is shown in Fig. 3.

temperature then dominates, pushing the transformation entropy back towards s_0 and thus decreasing the transformation strain in the process. Again, the full recovery of the transformation strain after the stress is removed is a fundamental feature of pseudoelastic behavior. The description in the section is meant to provide the motivation for the mathematical structure of the hardening potential. We now proceed to a more quantitative definition of the potentials and calculate the resulting thermomechanical behaviors from the solution of the model.

4.2. Specification of the hardening potential

The functions describing the hardening potential of Eq. (15) that are used in this model for a material that hardens during transformation have the following forms

$$\Psi_T^t = \frac{1}{2} H_T J_2^{t\,2} \frac{1}{\left(1 - \frac{\bar{\varepsilon}}{\varepsilon_0} - \frac{s^t}{s_0}\right)^{n_T}} \tag{28}$$

$$\Psi_C^t = \frac{1}{2} H_C J_2^{t\,2} \frac{1}{\left(1 - \frac{\bar{\varepsilon}}{\varepsilon_0} - \frac{s^t}{s_0}\right)^{n_C}} \tag{29}$$

Table 1
Material property values that are used to fit the experimental results in Esomat (2009).

Parameter (Unit)	Value	Parameter (Unit)	Value
E (GPa)	53	H_T (MPa)	108
θ_0 (K)	10	H_C (MPa)	864
ν	0.33	H_1^s (MPa)	1.65
σ_0 (MPa)	108	θ^t (K)	230
$\varepsilon_C^{sym}, \varepsilon_C^{asym}$	5.7%, 3%	H_2^s (K^2/MPa)	6.06
$\varepsilon_T^{sym}, \varepsilon_T^{asym}$	5.7%, 5.7%	n_T	0.6
a^{sym}, a^{asym}	0, 0.9979	n_C	0.01
s_0 ($\frac{\text{MPa}}{\text{K}}$)	0.33	u	0.005
α (K^{-1})	5.0E−5	v	0.0005

$$\Psi_s = H_1^s \frac{1}{\left(1 - \frac{s^t}{s_0}\right)^u \left(\frac{s^t}{s_0}\right)^v} + \theta^t s^t + \frac{1}{2} H_2^s s^{t\,2} \tag{30}$$

where H_T and H_C are the tension and compression hardening constants, and n_T and n_C are the tension and compression exponents that control the steepness of the asymptotic wall. Note that other forms of the tensile part of the hardening potential are used to model materials that soften during transformation in tension, and these will be described later.

The Ψ_s part of the hardening potential is a function that is dependent only on the transformation entropy and its purpose is primarily to set the stress-free temperature and entropy relationship. Notice that in Eq. (30) the denominator of the first term contains both $\left(1 - \frac{s^t}{s_0}\right)$ and $\frac{s^t}{s_0}$, which act as asymptotes that enforce the constraint that $0 < s^t < s_0$. At low temperature the transformation entropy is also low and the material is in the martensite phase, while at high temperature the transformation entropy is at its upper limit and the material is in the austenite phase. The remaining terms in Eq. (30) set the temperature where transformation occurs and the slope of the temperature–entropy response during the thermally induced phase transformation. Fig. 2 illustrates the form of Ψ_s chosen in this work along with points where isothermal stress–strain response will be reported.

The specification of the reversible behaviors, Eqs. (3) and (4), the flow rules, Eqs. (11) and (12), the transformation surface, Eq. (14), and the hardening potentials, Eqs. (15), (28), (29) and (30), allows

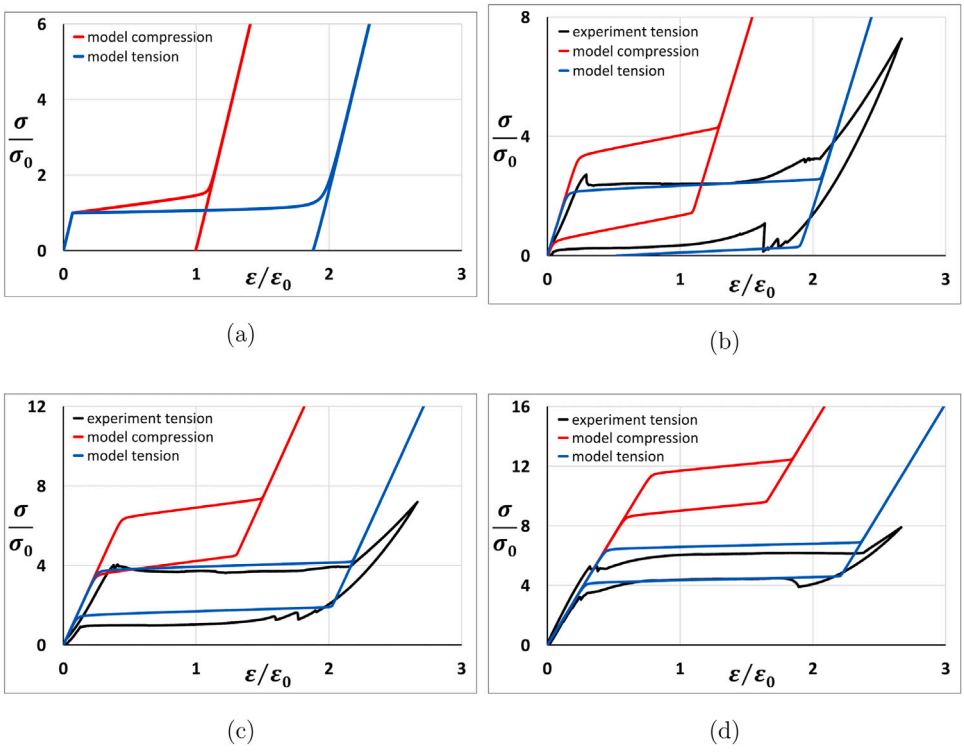

Fig. 3. Uniaxial tension σ-ε response for the following temperatures: (a) $\theta/\theta_0 = 5$ (b) $\theta/\theta_0 = 25.3$ (c) $\theta/\theta_0 = 28.3$ (d) $\theta/\theta_0 = 33.3$. The red curves for compression are only for the asymmetric version of the model. The compressive stress–strain response is identical to the tensile response for the symmetric version of the model. (For interpretation of the references to color in this figure legend, the reader is referred to the web version of this article.)

for the full solution of the model for the history of the strain and entropy given a history of stress and temperature. Here we choose model parameters, listed in Table 1, to fit the experimental stress–strain behaviors reported in the European Science Foundation EUROCORES Smart Structural Systems Technologies Roundrobin modeling effort Esomat (2009). Parameters for a model that is symmetric in tension versus compression are given along with an asymmetric version. Results are shown for uniaxial tests at temperatures of −20, 10, and 60 °C. Note that the compressive stress–strain responses are identical to the tensile responses for the symmetric version of the model, and so the red curves are only for the asymmetric model. A description of the qualitative effects of each parameter on the model behavior is included in Appendix A. Ultimately, the fits to the measured behavior are achieved by numerically integrating the model for a given thermo-mechanical loading history with a set of model parameters and then adjusting the parameters to achieve an improved representation of the experimental observations.

Fig. 3(a) shows the stress–strain behavior at constant temperature of $5\theta_0$. At this temperature the material is in the martensite phase, shown as point (a) on Fig. 2, and begins in a twinned martensite state. i.e. the transformation strain is zero. For such a state, the stress level where transformation occurs is actually set by the parameters of the transformation surface at the uniaxial stress level of σ_0. As transformation strain accumulates, the stress increases precipitously when the transformation strain approaches $\varepsilon_0/f(1)$, which is the saturation strain of the pure martensite phase in tension. Then when the stress is removed and returned to zero, the transformation strain persists and the material is left in a state of detwinned martensite.

Fig. 3(b) shows the stress–strain behavior at constant temperature of $25.3\theta_0$. In this state the material begins in the austenite phase at point (b) on Fig. 2, where the temperature is not significantly higher than the martensite to austenite finish temperature. Notice here that the stress level where transformation apparently begins in tension/(compression) is at approximately $2/(3.5)\sigma_0$, which means that this strength is not governed by the parameters of the transformation surface, but rather by the fact that the hardening potential creates a rapidly rising back stress for the very small but non-zero changes in transformation strain that do occur when the applied stress is greater than σ_0. In contrast to the case shown in Fig. 3(a), the plateau portion of the stress–strain behavior is driven by the austenite to martensite phase transition as opposed to martensite detwinning. Again, the transformation strain saturates at the level of $\varepsilon_0/f(1)$ at high stress levels where the material is in a state of stress-induced martensite.

Figs. 3(c) and 3(d) show the stress–strain behavior at constant temperatures of $28.3\theta_0$ and $33.3\theta_0$, shown as points (c) and (d) on Fig. 2 respectively. The features and description of the behavior at these temperatures mimic those provided for Fig. 3(b) at the temperature of $25.3\theta_0$. The difference being that the stress levels where transformation and reverse transformation occur are considerably higher than those at $25.3\theta_0$. This behavior is an illustration of the competition between the temperature driving the material towards the austenite phase and the stress driving the material towards the detwinned martensite phase that is encoded within the functional forms of the hardening potential. One final issue of note is that the "peaked" responses at the onset of forward and reverse transformation seen in the experimental observations are indicative of localized straining that is associated with a softening response in tension. However, the model using the parameters in Table 1 for comparison has a hardening behavior and thus does not capture such strain localizations. To do so requires a structural calculation with a constitutive description that allows for softening in tension Jiang et al. (2017b,c).

Next, results for multiaxial loading are presented. Fig. 4 shows results based on the constitutive model for the apparent transformation surface of the material. By "apparent" we are referring to how such a transformation surface would be defined in a laboratory setting as opposed to the model transformation surface that is defined in Eq. (14). These apparent transformation surfaces were obtained from simulations of proportional load paths in the $(\sigma_{11}, \sigma_{22})$ biaxial stress space. In each

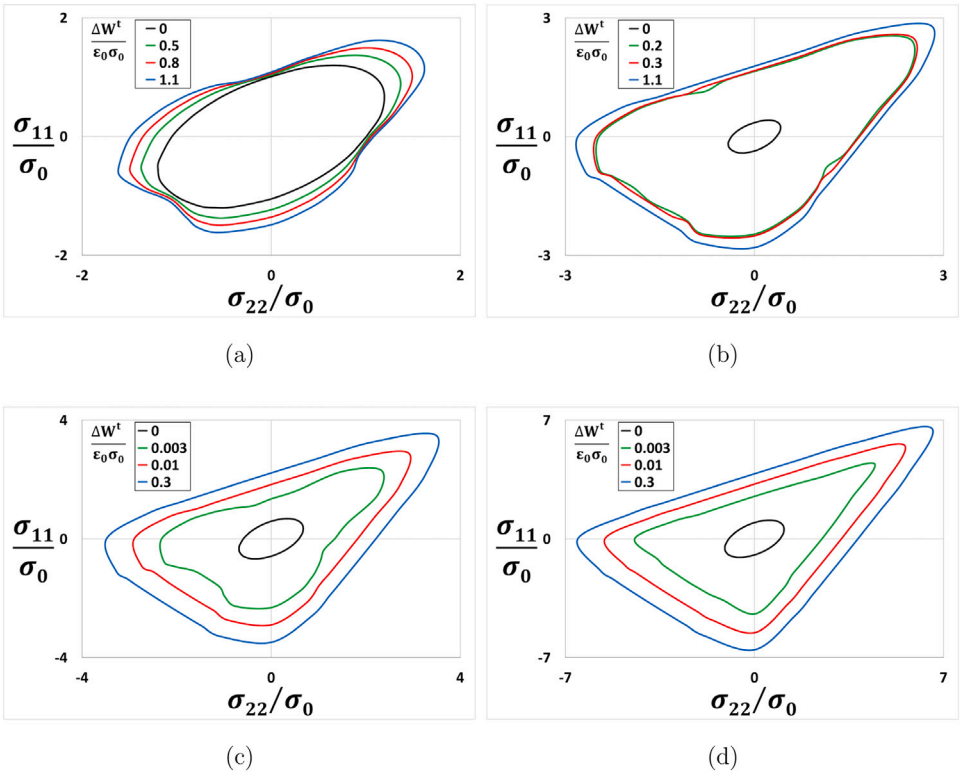

Fig. 4. Apparent surfaces for different values of transformation work for the following temperatures: (a) $\theta/\theta_0 = 12$ (b) $\theta/\theta_0 = 24.2$ (c) $\theta/\theta_0 = 25.3$ (d) $\theta/\theta_0 = 28.3$.

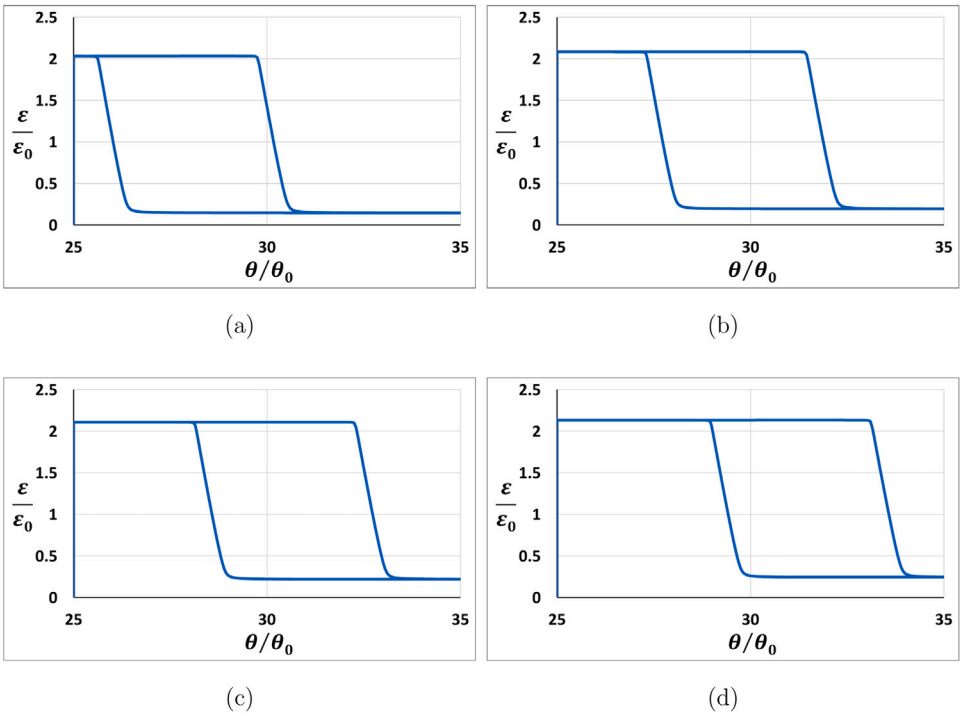

Fig. 5. Thermal cycling ε-θ response under constant tensile stress levels of: (a) $\sigma/\sigma_0 = 3$ (b) $\sigma/\sigma_0 = 4$ (c) $\sigma/\sigma_0 = 4.5$ (d) $\sigma/\sigma_0 = 5$.

simulation, the stresses are recorded for as a function of the transformation work, which is defined as $\Delta W^t = \int \sigma_{ij} d\varepsilon^t_{ij}$. Transformation surfaces are then constructed by plotting the stress levels achieved in each proportional loading simulation at different levels of the transformation work. There are several features of note.

First, the transformation surface at $\Delta W^t = 0$ is simply the J_2-type transformation surface defined in Eq. (14). Furthermore, especially at higher temperatures, this surface is small in comparison to the apparent transformation surfaces at measurable levels of the transformation work. This is due to the kinematic hardening nature of the model, as the center of this small surface moves around in stress space as

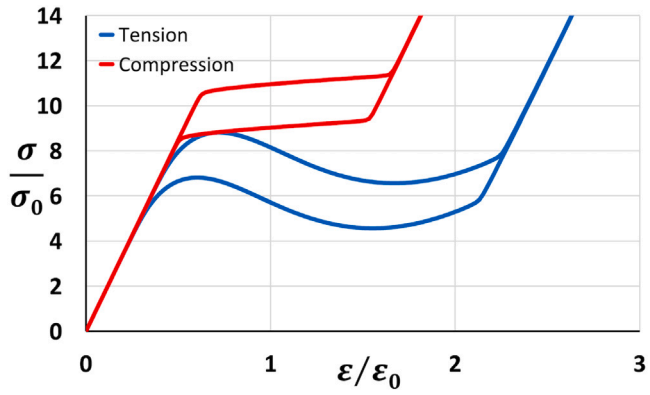

Fig. 6. Uniaxial tension and compression behaviors for a model material description given in Eq. (31) allowing for softening in tension but hardening in compression.

transformation strain accumulates, reverses, or reorients. Finally, the asymmetry in tension versus compression becomes readily apparent at higher temperatures, and even though the model transformation surface is purely J_2 based, the apparent transformation surfaces clearly display a strong dependence on the J_3 invariant of the effective stress. We note that this type of apparent transformation surface evolution has also been observed in micromechanics simulations Aleong et al. (2002), which offers qualitative support to this phenomenological formulation. Complementary to the stress–strain behavior at constant temperature shown in Fig. 3 are the strain versus temperature behaviors shown in Fig. 5. In these simulations the material is cooled to $25\theta_0$ at zero stress. Next, a uniaxial tension is applied until a maximum constant stress of (a) $3\sigma_0$, (b) $4\sigma_0$, (c) $4.5\sigma_0$, or (d) $5\sigma_0$ is applied. Next, heat is applied and withdrawn to cycle the temperature to a maximum of $35\theta_0$ and the strain is recorded. The figure illustrates how the stress creates an energetic preference for the martensite phase thus increasing the temperature required for the phase transition from martensite to austenite.

4.3. Softening in tension

A feature of SMA behavior, especially at temperatures in the pseudoelastic regime, is that the hardening in compression is generally larger than that in tension, and in fact there can be softening in tension, Hallai and Kyriakides (2013), Jiang et al. (2017a,b,c), Frost et al. (2019). To model such behavior the tensile part of the hardening potential Eq. (15) must be suitably modified. The tensile part of the hardening potential used to model softening in tension is given in Eq. (31), where H_0^s is the softening modulus that controls the amount of softening, and A is a constant that defines the behavior at low temperatures.

$$\bar{\mathcal{Y}}^t = \frac{1}{2} H_T J_2^{t2} \frac{\left(1-\left(\frac{s^t}{s_0}\right)^r\right)^p \left(H_0^s\left(\frac{s^t}{s_0}\right)^q + A\right)}{\left(1-\frac{s^t}{s_0}\right)\left(1-\frac{\bar{\varepsilon}}{\varepsilon_0}-\frac{s^t}{s_0}\right)^n + \frac{s^t}{s_0}\left(1-\frac{\bar{\varepsilon}}{\varepsilon_0}-\frac{s^t}{s_0}\right)^m} \tag{31}$$

The softening behavior is only applied to the tensile part of the hardening potential. The stress–strain hysteresis using this form of the tensile potential can be seen in Fig. 6 at a high temperature where the initial state is in the austenite phase. Such behavior is critical for modeling the phase transformation fronts that form and propagate through SMA structures, Jiang et al. (2017a,b,c), Frost et al. (2019).

4.4. Non-proportional loading

In this section the behavior of the model for a non-proportional loading path is presented. The model is compared to an experimental study reported by Helm and Haupt (2003). Helm and Haupt (2003) provides tensile stress–strain measurements on NiTi tubes, and the model presented here is fit to the uniaxial experimental results shown in Fig. 3(a) of Helm and Haupt (2003) with the parameters shown in Table 2. Note that the comparison provided here will use both a symmetric and an asymmetric version of the present model. Helm and Haupt (2003) do not provide any data on the compressive response of the material and so we have made the assumption of a strain asymmetry of $\varepsilon_T/\varepsilon_C = 1/f(1) = 1.8$ for the asymmetric case. Note that both the symmetric and asymmetric version have the same quality of fit to the experimentally measured uniaxial tension behavior. Fig. 7(a) shows the tension–torsion strain history imposed in the experiments of Helm and Haupt (2003). Fig. 7(b) then shows the predicted stress histories from the present model for both the symmetric and asymmetric representations, along with the experimental results. The response of the model shows that the symmetric representation underestimates the magnitudes of the shear and compressive stresses observed at the upper left corner of the experimental response, $\left(\sigma_{exp}, \sqrt{3}\tau_{exp}\right) = (-150, 310)$ MPa. However, the present model with a strain asymmetry of $\varepsilon_T/\varepsilon_C = 1.8$, which is characteristic of NiTi, is able to reproduce these values. It is also worth noting that the experimental result does differ quantitatively with the simulations of both models. One of the reasons for such a departure is that tube materials almost always contain crystallographic texture which causes anisotropy in the transformation behavior between the longitudinal and hoop directions. Such anisotropy is not accounted for in this model description, and is beyond the scope of the present work.

Table 2
Material property values that are used to fit the experimental observations in Helm and Haupt (2003).

Parameter (Unit)	Value	Parameter (Unit)	Value
E (GPa)	43	H_T (MPa)	0.75
θ_0 (K)	10	H_C (MPa)	0.75
ν	0.086	H_1^s (MPa)	1.5
σ_0 (MPa)	75	θ^t (K)	258
$\varepsilon_C^{sym}, \varepsilon_C^{asym}$	4.9%, 2.73%	H_2^s (K^2/MPa)	1.67
$\varepsilon_T^{sym}, \varepsilon_T^{asym}$	4.9%, 4.9%	n_T	0.6
a^{sym}, a^{asym}	0, 0.990	n_C	0.6
s_0 ($\frac{\text{MPa}}{\text{K}}$)	0.3	u	0.005
α (K^{-1})	5.0E−5	v	0.0005

In addition to the results of Helm and Haupt (2003), we also compare the present model to the experimental results on solid SMA wires from the European Science Foundation EUROCORES Smart Structural Systems Technologies Roundrobin modeling effort Esomat (2009). Here, the material properties are the same as those used in Table 1 for the asymmetric model. A symmetric model was also constructed to fit the tensile response provided in the measurements. Note that these simulations on wires require a structural simulation where the constitutive model is integrated at multiple points along the radius of the wire. These simulations are carried out at a fixed temperature, axial force is applied to the wire, held fixed, and then a twist angle is applied to the wire and cycled in both directions. Fig. 8 shows a comparison of the symmetric and asymmetric models to the experimental observations. Note that for the high temperature case with $T = 30$ °C, the reported data did not include the initial axial strain associated with the applied 70 MPa stress. As such, this data has been adjusted upward by the strain amount corresponding to the measured elastic modulus. Fig. 8 shows that both the symmetric and asymmetric models underestimate the magnitude of the torque during twist cycling, but the asymmetric model performs better than the symmetric model. For the axial strain response during twist cycling, the asymmetric model tends to overestimate the axial strain for the two higher temperature cases and the symmetric model tends to underestimate the axial strain for the highest temperature case.

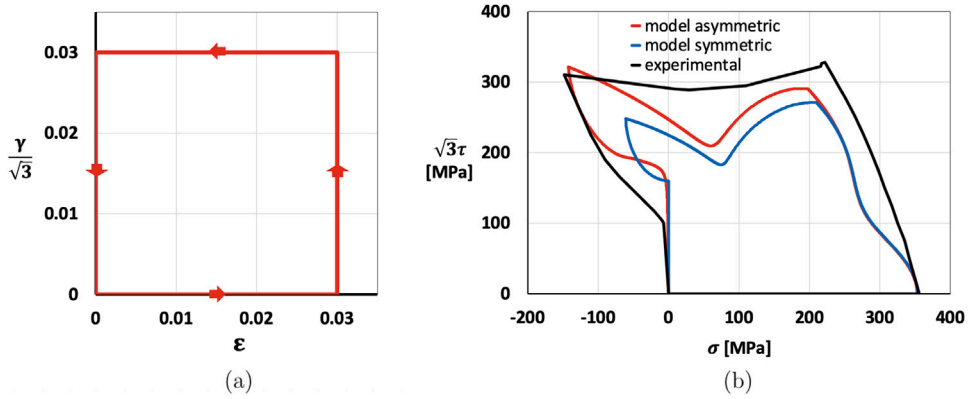

Fig. 7. Stress predictions of the model for a non-proportional rectangular tension–torsion loading path under strain control. Experimental results for such a path are given in Helm and Haupt (2003). The imposed strain history is shown in (a), and the resulting stress history for both a symmetric ($\varepsilon_T/\varepsilon_C = 1/f(1) = 1$) and an asymmetric ($\varepsilon_T/\varepsilon_C = 1/f(1) = 1.8$) version of the present model is shown in (b).

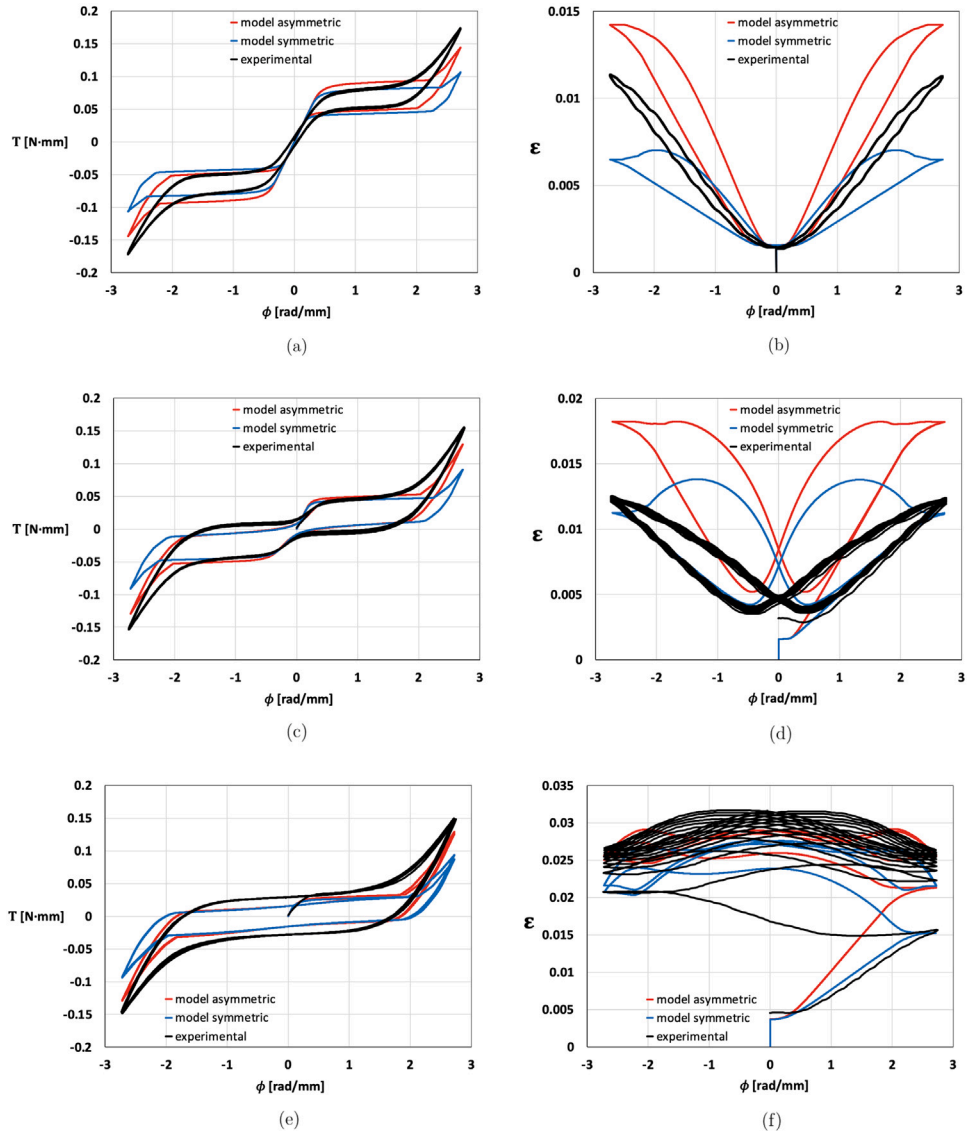

Fig. 8. Torque versus twist and axial strain versus twist predictions of the model for a non-proportional tension–torsion loading cycle on an SMA wire. The torque versus angular displacement and axial strain vs angular displacement are shown in (a)–(b) for $\theta = 30\,°C$, (c)–(d) for $\theta = -10\,°C$, and (e)–(f) for $\theta = -30\,°C$. The predictions are for both a symmetric ($\varepsilon_T/\varepsilon_C = 1/f(1) = 1$) and asymmetric ($\varepsilon_T/\varepsilon_C = 1/f(1) = 1.9$) versions of the present model.

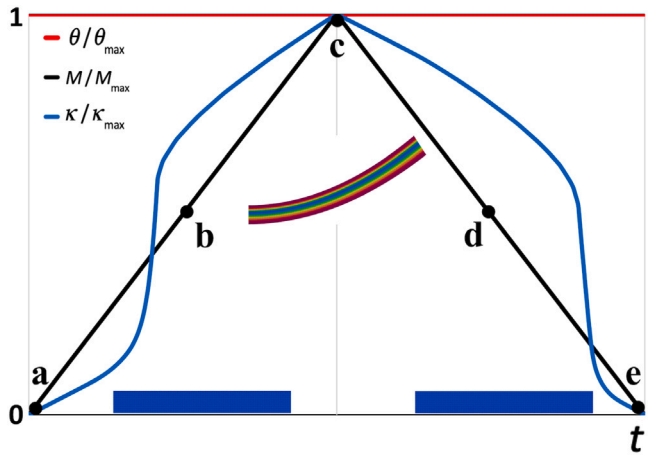

Fig. 9. The thermal and mechanical loading history for the high temperature pseudoelastic case. The temperature is fixed at $\theta/\theta_0 = \theta_{max}/\theta_0 = 33.3$. The effective strain $\bar{\varepsilon}$ is shown as color contours on the deformed shape of the beam at states **a**, **c**, and **e**. A plot of the moment–curvature response is shown in Fig. 10. The axial stress distributions through the cross-section for stated **a**-**e** are shown in Fig. 11.

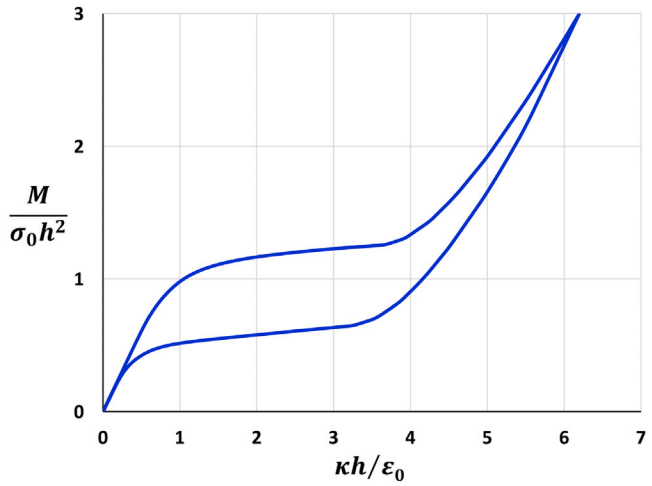

Fig. 10. The moment–curvature behavior for pure bending of an SMA beam. In this case the temperature is held at $\theta/\theta_0 = 33.3$, and for comparison the austenite to martensite transition temperature is approximately $\theta/\theta_0 = 23$.

5. Finite element analysis of an SMA beam

The purpose of phenomenological constitutive models such as this one is for use in finite element calculations of SMA structures, Jiang and Landis (2016), Jiang et al. (2016, 2017a,b,c), Frost et al. (2016, 2019). Here we present simulations of bending and recovery, either due to the pseudoelastic effect at high temperature or due to the shape memory effect, of an SMA beam. These calculations assume small deformations and are based on the incremental form of the principal of virtual work which is then solved iteratively with a multi-dimensional Newton–Raphson method. The method requires both a technique for integrating the constitutive model at each integration point in the finite element domain along with the determination of the algorithmically consistent tangent moduli at each of these points. The constitutive integration technique is a backward Euler method that is described in the Appendix and leads to a symmetric consistent tangent stiffness, also provided in the Appendix. Although it is not necessary to simulate a long beam for such pure bending simulations when the material hardens in both tension and compression, the length of the beam was taken to be 10 times its height, h. For the pseudoelastic beam simulation, Fig. 9, plane stress conditions are assumed and the temperature is held fixed at a high level of $\theta/\theta_0 = 33.3$ throughout the loading history such that the simulation is isothermal in both time and spatially. The left end of the beam has zero horizontal displacements imposed, and the right end has a moment M applied while the surface is constrained to remain a plane using multi-point constraints such that the net horizontal force applied to the beam is zero. Fig. 9 shows both the thermal and mechanical loading history that is applied as a function of time along with the computed curvature response of the beam and contour plots of $\bar{\varepsilon}$ superimposed on the deformed configuration of the beam at load-points **a**, **c**, and **e**.

Fig. 10 shows the moment–curvature relationship for the beam subjected to the thermomechanical loading history shown in Fig. 9. We note that both the tensile and compressive behaviors harden throughout the full strain history and so there are no localized deformations or transformation fronts as seen in the experiments and simulations of Jiang and Landis (2016), Jiang et al. (2016, 2017a,b,c), wherein the material softened in tension. Such softening behaviors lead to a plateau in the moment–curvature relationship and to interesting patterns of non-uniform deformation. In contrast, for a purely hardening material like the one used in this simulation, the stress and deformation fields only depend on the distance from the neutral axis in the beam.

However even though the fields are well-behaved, due to the asymmetry in tension versus compression, there is also an asymmetry in the axial stress distribution through the cross-section of the beam as shown in Fig. 11. Here the axial stress distributions as a function of the distance from the centerline of the beam are shown for both loading and unloading. The differences in the distributions between states **b** and **d** are illustrative of the hysteresis in the material behavior. Note the differences in the distributions of axial stress on the tensile and compressive sides of the beam, with the stress levels on the compressive side higher than those on the tensile side. This feature also moves the neutral axis of the beam from the center towards the compressive side of the beam.

Next, Fig. 12 shows a thermomechanical loading history designed to illustrate the structural shape memory effect for the SMA beam. In this simulation the bending moment loading is applied to deform the beam at low temperature, $\theta = 20\theta_0$ (recall that the austenite to martensite transition temperature is $\theta_c = 23\theta_0$). The end moment is then removed at the same temperature leaving the beam in a deformed state **e** while unloaded, i.e. the beam curvature is non-zero but the applied moment is zero. Fig. 13(a) shows the moment–curvature response during this first loading and unloading phase of the simulation. The beam is then heated at zero applied moment such that the deformation is recovered, and then the beam is cooled back down to its initial temperature. Fig. 13(b) shows the curvature–temperature response of the beam during this thermal loading and unloading phase of the simulation. Note that in this case, the thermal loading is not isothermal in time, but it is spatially isothermal in that at each instant in time the temperature is uniform throughout the beam and no heat conduction is required to equilibrate the temperature. In other words, the temperature history at all material points in the beam is specified during the all phases of the simulation.

Fig. 14 plots the axial stress distribution through the cross-section of the beam for different points on the thermo-mechanical loading history shown in Fig. 12. Fig. 14(a) shows the distributions of axial stress during the mechanical loading at points **a**, **b**, and **c** in Fig. 12. Notice that there is still asymmetry in the tensile versus compressive strains for the material, but that the asymmetry in the stress levels is significantly less pronounced than those for the pseudoelastic case. Fig. 14(b) shows the distributions during the mechanical unloading at points **c**, **d**, and **e** in Fig. 12. Again, the asymmetry is less pronounced in this case, but remains apparent. Finally, Fig. 14(c) shows the distributions of axial stress during the thermal loading and unloading at points **e**, **f**, and **g** on

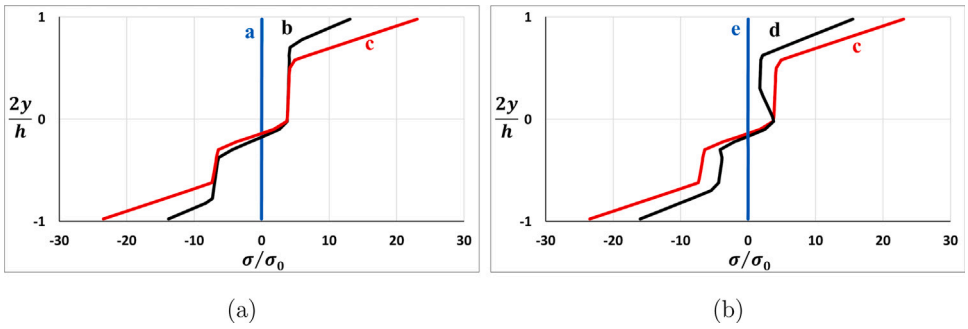

Fig. 11. The axial stress distributions through the cross-section for (a) loading to states **a**, **b**, and **c** as shown in Fig. 9, and (b) unloading from state **c** to **d** and **e**.

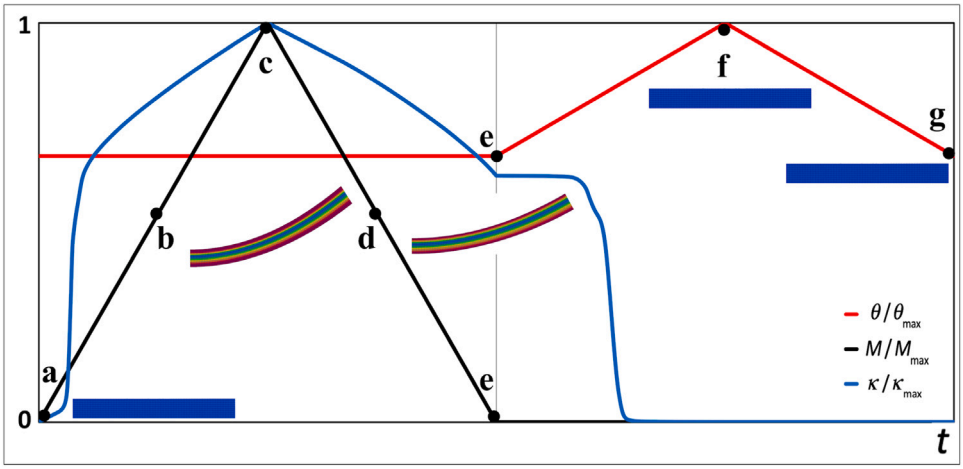

Fig. 12. The thermal and mechanical loading history imposed on the SMA beam to illustrate the shape memory effect. The temperature is held fixed in the first phase while the beam is loaded and then unloaded by a bending moment. The temperature is then raised causing the martensite to austenite transition leading to the recovery of the original beam shape. The temperature is then reduced back to the original state with the beam returned to the martensite phase and its original shape. The insets show the deformed shape of the beam with the effective transformation strain superposed as color contours. (For interpretation of the references to color in this figure legend, the reader is referred to the web version of this article.)

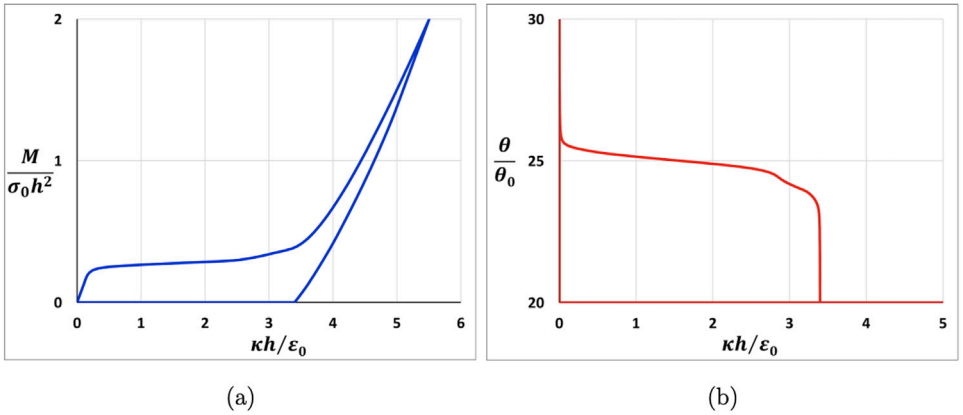

Fig. 13. The moment–curvature and temperature–curvature behavior for pure bending of an SMA beam. In this case the full thermo-mechanical loading history is shown in Fig. 12. Recall that the austenite to martensite transition temperature is approximately $\theta/\theta_0 = 23$.

Fig. 12 with the distributions at states **f** and **g** overlapping one another due to the recovery of the initial beam shape at high temperature.

6. Discussion

A new phenomenological constitutive law for the thermomechanical behavior of shape memory alloys has been presented based on a constitutive modeling structure that implements a single transformation surface to account for the forward martensite to austenite phase transformation, the reverse austenite to martensite phase transformation, and for the reorientation of martensite during non-proportional stress histories. These seemingly disparate processes are accounted for via the construction of a hardening potential that depends on the internal variables of transformation strain and transformation entropy. The hardening potential is then used to derive back stresses and back temperatures that define the location of the center of the transformation surface in stress–temperature space. The size of the transformation

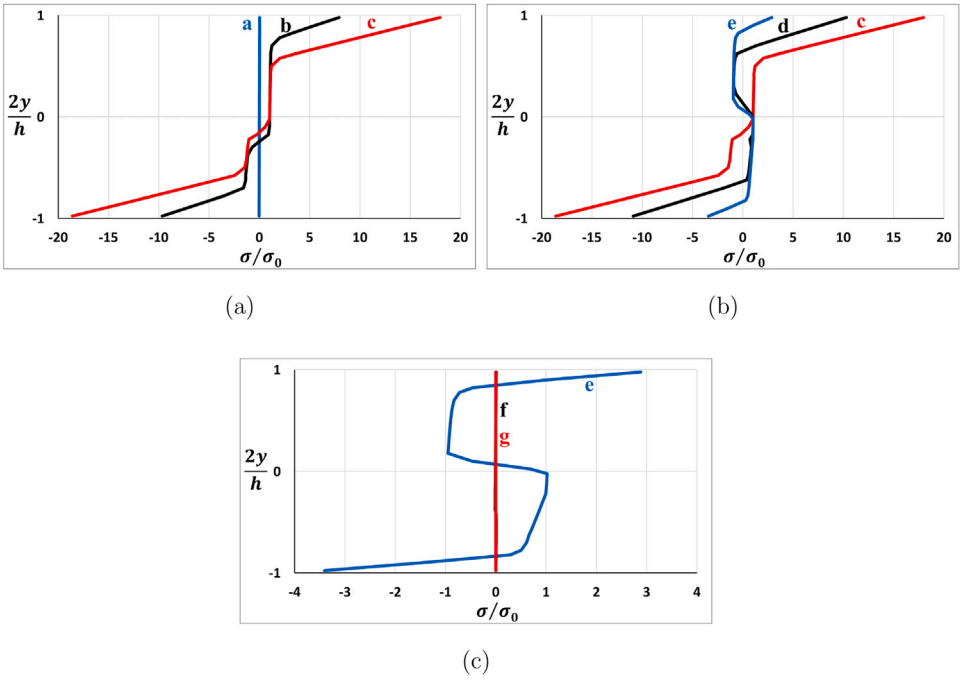

Fig. 14. (a) The distributions of axial stress during the mechanical loading at points **a**, **b**, and **c** in Fig. 12. (b) The distributions during the mechanical unloading at points **c**, **d**, and **e**. (c) The distributions during the thermal loading and unloading at points **e**, **f**, and **g**. Note that the distributions of stress at states **f** and **g** overlap one another in (c).

surface is responsible for the size of the mechanical and thermal hysteresis, while the features of the hardening potential are responsible for the stress and temperature levels where significant amounts of transformation strain and/or phase changes accumulate.

The construction of the hardening potential based on on the admissible states of the internal variables was described and asymptotes surrounding the boundary of the admissible state space were used to enforce the constraints on the internal variables. For example, the transformation entropy, which is a surrogate for the martensite volume fraction, is constrained to lie between its minimum and maximum values for martensite and austenite respectively. Furthermore, the transformation strain has analogous limits which have been characterized by an effective transformation strain variable, $\bar{\varepsilon}$. Parameter values entering into the proposed functional forms of the hardening potential characteristic of NiTi were provided for both a hardening and a softening material.

Phenomenological constitutive laws such as this one are most useful for numerical calculations of the thermo-mechanical response of SMA structures and devices. Along these lines, the proposed constitutive model was implemented within finite element calculations to simulate the structural response of a simple beam subjected to a pure bending moment under plane stress conditions. The numerical integration routine for the constitutive model along with the consistent tangent moduli are given in the Appendices. The beam simulations show both the pseudoelastic response of the structure at high temperature along with the shape recovery behavior of a deformed martensite beam subjected to an increase in temperature. In this work linear kinematics was assumed, however the model can readily be extended to finite deformation using the same procedures outlined in Xu et al. (2019) to account for large deformations and rotations.

In conclusion, the approach presented here, based on a single transformation surface, is arguably simpler than those that define multiple surfaces for each mechanism of transformation, forward martensite to austenite, backward austenite to twinned or detwinned martensite, and reorientation of martensite. The mathematical structure of the theory is that of a kinematic hardening plasticity theory with an associated flow rule and back stresses derived from an energetic hardening potential. The simplicity of the theoretical structure lends itself to implementation in finite element calculations of the physical behaviors of SMA devices.

Declaration of competing interest

The authors declare that they have no known competing financial interests or personal relationships that could have appeared to influence the work reported in this paper.

Acknowledgment

The authors acknowledge with thanks the financial support received for this work from the National Science Foundation under grant no. CMMI-1762389.

Appendix A. Calibration

Here we describe the procedure that has been used to fit the model to experimental measurements. Given the non-linear and irreversible nature of the model, ultimately the best fits are achieved by numerically integrating the model for the experimental thermo-mechanical loading history with a set of parameters and then adjusting the parameters to achieve an improved fit. Due to the nonlinear description of the hardening potential Ψ^t it is not always possible to decouple all of the parameters such that they can be fit to one specific aspect of the measured response, although some of the parameters do have such a simple physical link.

We begin with the reversible properties. Note that the theory allows for all of the reversible properties to be anisotropic and also to depend on the internal variables, s^t and ε^t_{ij}. However, in this work we assume isotropic properties and do not attempt to model any differences in the properties between martensite and austenite. Hence, E, ν, α, and C are the Young's modulus, Poisson's ratio, thermal expansion coefficient, and specific heat per unit volume at fixed strain. Generally, the mechanical properties are taken from high temperature stress–strain curves, and the thermal expansion and specific heat is taken as an average between the martensite and austenite phases when the simplifying

assumptions described above are used. Note that α and C do not play a significant role in any of the behaviors discussed in this paper.

Next, the parameters appearing in the thermal part of the hardening potential of Eq. (30) and the size of the thermal hysteresis should be taken from thermal measurements of the temperature and heat input/output response of the material. The width of the thermal hysteresis along the temperature axis during a full stress-free excursion from austenite to martensite and back is equal to $2\theta_0$ in this model. The other properties are closely related to features of the back temperature and transformation entropy shown in Fig. 2. First, the transformation temperature between martensite and austenite can be defined from the $\theta^B - s^t$ curve as the value of θ^B when $s^t = 0.5 s_0$, which is directly controlled by (although not exactly equal to) the model parameter θ^t appearing in Eq. (30). As discussed in the text, the parameter $s_0 = s_A - s_M$, where s_A and s_M are the entropy per unit volume of the pure austenite and pure martensite phases respectively. The latent heat of transformation, Q_L, given as the heat absorbed by a unit volume of material during the transformation from pure martensite to pure austenite, is the area under the $\theta^B - s^t$ curve and is approximately given as $Q_L \approx s_0 \theta^t$. The slope of the shallow-sloped portion of the $\theta^B - s^t$ curve shown in Fig. 2 is controlled primarily by the parameter H_2^s, which also controls the differences between the martensite/austenite start and finish temperatures. The "sharpness" of the transitions between the asymptotes and the shallow-sloped portion of this curve where $s^t \to 0$ and $s^t \to s_0$ are controlled by the parameters u and v, with smaller values leading to sharper kinks in the transitions. u and v also affect the kink-like transitions in the stress–strain behavior. The remaining coefficient in Eq. (30), H_1^s, controls the steepness of the asymptotes as $s^t \to 0$ and $s^t \to s_0$.

The final set of properties that are of interest include the possible transformation strains in tension/compression, the size of the mechanical hysteresis, and the mechanical hardening parameters of Eqs. (28) and (29). In this work, twinned martensite that has been cooled from the austenite phase without applied loading is used as the reference strain state, and this is common to all macroscopic phenomenological models that neglect the volume change difference between austenite and martensite. The parameter $\varepsilon_0 = \varepsilon_C$ is the transformation strain that can be achieved by pure martensite loaded by a high uniaxial compressive stress, and $\varepsilon_0 / f(1) = \varepsilon_T$ is the transformation strain that can be achieved by pure martensite loaded by a high uniaxial tensile stress. Given the ansatz of Eq. (21), these two quantities set the value of a. As explained in the main body of this paper, the size of the mechanical hysteresis along the stress axis in a uniaxial stress–strain test at low temperature is equal to $2\sigma_0$. Lastly, the parameters H_T, H_C, n_T, and n_C, are implemented to control the shallow-sloped part of the stress–strain behavior along with the temperature dependence of the apparent transformation stress. The nonlinear nature of Eqs. (28) and (29) and the structure of the model in general make it difficult to deconvolve the dependence of the model response on these properties in an analytical manner, and so simulations are performed in order to find the combinations of these parameters that yield good fits to the observed material response.

Appendix B. Integration routine

Let $\left(\sigma_{ij}^n, \varepsilon_{ij}^n, \varepsilon_{ij}^{t,n}, \theta^n, s^{t,n}\right)$ represent the stress, strain, transformation strain, temperature, and transformation entropy at time t_n, and $\left(\Delta\varepsilon_{ij}^{n+1}, \Delta\theta^{n+1}\right)$ are the strain increment and temperature increment at time t_{n+1}. Therefore, the following variables can be computed at time t_{n+1} and for simplicity the notation $n+1$ that appear at time t_{n+1} will be dropped:

$$\varepsilon_{ij} = \varepsilon_{ij}^n + \Delta\varepsilon_{ij} \tag{B.1}$$

$$\theta = \theta^n + \Delta\theta \tag{B.2}$$

$$\sigma_{ij} = c_{ijkl}\left(\varepsilon_{kl} - \varepsilon_{kl}^{t,n} - \Delta\varepsilon_{kl}^t\right) - \beta_{ij}\theta \tag{B.3}$$

$$\Phi = \frac{3}{2}\frac{\hat{s}_{ij}\hat{s}_{ij}}{\sigma_0^2} + \frac{\hat{\theta}^2}{\theta_0^2} - 1 \tag{B.4}$$

$$\Delta\varepsilon_{ij}^t = 3\lambda\frac{\hat{s}_{ij}}{\sigma_0^2} \tag{B.5}$$

$$\Delta s^t = 2\lambda\frac{\hat{\theta}}{\theta_0^2} \tag{B.6}$$

The solver uses the backward Euler routine to discretize the constitutive equations which are then solved by a NR scheme. The above Eqs. (B.3), (B.4), (B.5), (B.6) are solved using the NR scheme that starts with initial guesses at time t and iteration $i = 0$ of $\Delta\varepsilon_{ij}^{t(0)}$ and $\Delta s^{t(0)}$. For a specific iteration (i), the following residuals r_{ij}, r_s, and r_λ from Eqs. (B.4), (B.5) and (B.6) have to satisfy the norm of residual defined as

$$\|r\| = \sqrt{r_{11}^2 + r_{22}^2 + r_{33}^2 + r_{12}^2 + r_{13}^2 + r_{23}^2 + r_s^2 + r_\lambda^2} \tag{B.7}$$

$$r_{ij} = -\Delta\varepsilon_{ij}^t + \frac{3\lambda}{\sigma_0^2}\hat{s}_{ij} \tag{B.8}$$

$$r_s = -\Delta s^t + \frac{2\lambda}{\theta_0^2}\hat{\theta} \tag{B.9}$$

$$r_\lambda = -\Phi \tag{B.10}$$

Check if $\left\|r^{(i)}\right\| \le TOL$, where TOL is the tolerance of convergence which in this case is 1.0×10^{-9}. If the initial guesses are satisfied then the solution is accepted for $\Delta\varepsilon_{ij}^{t^{(i)}}$ and $\Delta s^{t^{(i)}}$, otherwise calculate the increments of the unknowns $d\varepsilon_{kl}^{t^{(i)}}$ and $ds^{t^{(i)}}$ by solving

$$r_{ij}^{(i)} = J_{ijkl}^{(i)} d\varepsilon_{kl}^{t^{(i)}} + q_{ij}^{(i)} ds^{t^{(i)}} + n_{ij}^{(i)} d\lambda^{(i)} \tag{B.11}$$

$$r_s^{(i)} = p_{kl}^{(i)} d\varepsilon_{kl}^{t^{(i)}} + A^{(i)} ds^{t^{(i)}} + B^{(i)} d\lambda^{(i)} \tag{B.12}$$

$$r_\lambda^{(i)} = m_{kl}^{(i)} \varepsilon_{kl}^{t^{(i)}} + C^{(i)} ds^{t^{(i)}} + D^{(i)} d\lambda^{(i)} \tag{B.13}$$

$$J_{ijkl} = -\frac{\partial r_{ij}}{\partial \Delta\varepsilon_{kl}^t} = \left(\frac{1}{2} + \frac{3\lambda\mu}{\sigma_0^2}\right)\left(\delta_{ik}\delta_{jl} + \delta_{il}\delta_{jk}\right) + \frac{3\lambda}{\sigma_0^2} H_{ijkl}^{\sigma\sigma} \tag{B.14}$$

$$q_{ij} = -\frac{\partial r_{ij}}{\partial \Delta s^t} = \frac{3\lambda}{\sigma_0^2} H_{ij}^{\sigma\theta} \tag{B.15}$$

$$n_{ij} = -\frac{\partial r_{ij}}{\partial \lambda} = -\frac{3}{\sigma_0^2}\hat{s}_{ij} \tag{B.16}$$

$$p_{kl} = -\frac{\partial r_s}{\partial \Delta\varepsilon_{kl}^t} = \frac{2\lambda}{\theta_0^2}\frac{\partial\theta^B}{\partial\varepsilon_{kl}^t} \tag{B.17}$$

$$A = -\frac{\partial r_s}{\partial \Delta s^t} = 1 + \frac{2\lambda}{\theta_0^2}\frac{\partial\theta^B}{\partial s^t} \tag{B.18}$$

$$B = -\frac{\partial r_s}{\partial \lambda} = -\frac{2}{\theta_0^2}\hat{\theta} \tag{B.19}$$

$$m_{kl} = -\frac{\partial r_\lambda}{\partial \Delta\varepsilon_{kl}^t} = -\left(\frac{3}{\sigma_0^2}\hat{s}_{ij} H_{ijkl}^{\sigma\sigma} + \frac{2}{\theta_0^2}\hat{\theta} H_{ij}^{\theta\sigma}\right) \tag{B.20}$$

$$C = -\frac{\partial r_\lambda}{\partial \Delta s^t} = -\left(\frac{3}{\sigma_0^2}\hat{s}_{ij} H_{ij}^{\sigma\theta} + \frac{2}{\theta_0^2}\hat{\theta} H^{\theta\theta}\right) \tag{B.21}$$

$$D = -\frac{\partial r_\lambda}{\partial \lambda} = 0 \tag{B.22}$$

and then calculate the new $\Delta\varepsilon_{kl}^{t^{(i+1)}} = \Delta\varepsilon_{kl}^{t^{(i)}} + d\varepsilon_{kl}^{t^{(i)}}$, $\Delta s^{t^{(i+1)}} = \Delta s^{t^{(i)}} + ds^{t^{(i)}}$, $\lambda^{(i+1)} = \lambda^{(i)} + d\lambda^{(i)}$ and replace $i \to i+1$. This can be illustrated by assembling Eqs. (B.11), (B.12) and (B.13) into the following matrix form and solving for $d\varepsilon_{ij}^{t^{(i)}}$, $ds^{t^{(i)}}$, and $d\lambda^{(i)}$ (see Box I)

$$\begin{bmatrix} r_{11}^{(i)} \\ r_{22}^{(i)} \\ r_{33}^{(i)} \\ r_{12}^{(i)} + r_{21}^{(i)} \\ r_{13}^{(i)} + r_{31}^{(i)} \\ r_{23}^{(i)} + r_{32}^{(i)} \\ r_{s}^{(i)} \\ r_{\lambda}^{(i)} \end{bmatrix} = \begin{bmatrix} J_{1111}^{(i)} & J_{1122}^{(i)} & J_{1133}^{(i)} & 2J_{1112}^{(i)} & 2J_{1113}^{(i)} & 2J_{1123}^{(i)} & q_{11}^{(i)} & n_{11}^{(i)} \\ J_{2211}^{(i)} & J_{2222}^{(i)} & J_{2233}^{(i)} & 2J_{2212}^{(i)} & 2J_{2213}^{(i)} & 2J_{2223}^{(i)} & q_{22}^{(i)} & n_{22}^{(i)} \\ J_{3311}^{(i)} & J_{3322}^{(i)} & J_{3333}^{(i)} & 2J_{3312}^{(i)} & 2J_{3313}^{(i)} & 2J_{3323}^{(i)} & q_{33}^{(i)} & n_{33}^{(i)} \\ 2J_{1211}^{(i)} & 2J_{1222}^{(i)} & 2J_{1233}^{(i)} & 4J_{1212}^{(i)} & 4J_{1213}^{(i)} & 4J_{1223}^{(i)} & 2q_{12}^{(i)} & 2n_{12}^{(i)} \\ 2J_{1311}^{(i)} & 2J_{1322}^{(i)} & 2J_{1333}^{(i)} & 4J_{1312}^{(i)} & 4J_{1313}^{(i)} & 4J_{1323}^{(i)} & 2q_{13}^{(i)} & 2n_{13}^{(i)} \\ 2J_{2311}^{(i)} & 2J_{2322}^{(i)} & 2J_{2333}^{(i)} & 4J_{2312}^{(i)} & 4J_{2313}^{(i)} & 4J_{2323}^{(i)} & 2q_{23}^{(i)} & 2n_{23}^{(i)} \\ p_{11}^{(i)} & p_{22}^{(i)} & p_{33}^{(i)} & 2p_{12}^{(i)} & 2p_{13}^{(i)} & 2p_{23}^{(i)} & A^{(i)} & B^{(i)} \\ m_{11}^{(i)} & m_{22}^{(i)} & m_{33}^{(i)} & 2m_{12}^{(i)} & 2m_{13}^{(i)} & 2m_{23}^{(i)} & C^{(i)} & D^{(i)} \end{bmatrix} \begin{bmatrix} d\varepsilon_{11}^{t(i)} \\ d\varepsilon_{22}^{t(i)} \\ d\varepsilon_{33}^{t(i)} \\ d\varepsilon_{12}^{t(i)} \\ d\varepsilon_{13}^{t(i)} \\ d\varepsilon_{23}^{t(i)} \\ ds^{t(i)} \\ d\lambda^{(i)} \end{bmatrix} \tag{B.23}$$

Box I.

$$\begin{aligned} H_{ijkl}^{\sigma\sigma} = \xi \Bigg(& \frac{\partial^2 \Psi_C^t}{\partial \bar{\varepsilon}^2} \frac{\partial \bar{\varepsilon}}{\partial \varepsilon_{ij}^t} \frac{\partial \bar{\varepsilon}}{\partial \varepsilon_{kl}^t} + \frac{\partial \Psi_C^t}{\partial \bar{\varepsilon}} \frac{\partial^2 \bar{\varepsilon}}{\partial \varepsilon_{ij}^t \partial \varepsilon_{kl}^t} + \frac{\partial^2 \Psi_C^t}{\partial J_2^{t2}} \frac{\partial J_2^t}{\partial \varepsilon_{ij}^t} \frac{\partial J_2^t}{\partial \varepsilon_{kl}^t} + \frac{\partial \Psi_C^t}{\partial J_2^t} \frac{\partial^2 J_2^t}{\partial \varepsilon_{ij}^t \varepsilon_{kl}^t} \\ & + \frac{\partial^2 \Psi_C^t}{\partial \bar{\varepsilon} \partial J_2^t} \left(\frac{\partial J_2^t}{\partial \varepsilon_{ij}^t} \frac{\partial \bar{\varepsilon}}{\partial \varepsilon_{kl}^t} + \frac{\partial J_2^t}{\partial \varepsilon_{kl}^t} \frac{\partial \bar{\varepsilon}}{\partial \varepsilon_{ij}^t} \right) \Bigg) + \frac{\partial \xi}{\partial \varepsilon_{kl}^t} \left(\frac{\partial \Psi_C^t}{\partial \bar{\varepsilon}} \frac{\partial \bar{\varepsilon}}{\partial \varepsilon_{ij}^t} + \frac{\partial \Psi_C^t}{\partial J_2^t} \frac{\partial J_2^t}{\partial \varepsilon_{ij}^t} \right) \\ & + \frac{\partial \xi}{\partial \varepsilon_{ij}^t} \left(\frac{\partial \Psi_C^t}{\partial \bar{\varepsilon}} \frac{\partial \bar{\varepsilon}}{\partial \varepsilon_{kl}^t} + \frac{\partial \Psi_C^t}{\partial J_2^t} \frac{\partial J_2^t}{\partial \varepsilon_{kl}^t} \right) + \frac{\partial^2 \xi}{\partial \varepsilon_{ij}^t \partial \varepsilon_{kl}^t} \Psi_C^t \\ & + (1-\xi) \Bigg(\frac{\partial^2 \Psi_T^t}{\partial \bar{\varepsilon}^2} \frac{\partial \bar{\varepsilon}}{\partial \varepsilon_{ij}^t} \frac{\partial \bar{\varepsilon}}{\partial \varepsilon_{kl}^t} + \frac{\partial \Psi_T^t}{\partial \bar{\varepsilon}} \frac{\partial^2 \bar{\varepsilon}}{\partial \varepsilon_{ij}^t \partial \varepsilon_{kl}^t} + \frac{\partial^2 \Psi_T^t}{\partial J_2^{t2}} \frac{\partial J_2^t}{\partial \varepsilon_{ij}^t} \frac{\partial J_2^t}{\partial \varepsilon_{kl}^t} + \frac{\partial \Psi_T^t}{\partial J_2^t} \frac{\partial^2 J_2^t}{\partial \varepsilon_{ij}^t \varepsilon_{kl}^t} \\ & \frac{\partial^2 \Psi_T^t}{\partial \bar{\varepsilon} \partial J_2^t} \left(\frac{\partial J_2^t}{\partial \varepsilon_{ij}^t} \frac{\partial \bar{\varepsilon}}{\partial \varepsilon_{kl}^t} + \frac{\partial J_2^t}{\partial \varepsilon_{kl}^t} \frac{\partial \bar{\varepsilon}}{\partial \varepsilon_{ij}^t} \right) \Bigg) + \frac{\partial \xi}{\partial \varepsilon_{kl}^t} \left(\frac{\partial \Psi_T^t}{\partial \bar{\varepsilon}} \frac{\partial \bar{\varepsilon}}{\partial \varepsilon_{ij}^t} + \frac{\partial \Psi_T^t}{\partial J_2^t} \frac{\partial J_2^t}{\partial \varepsilon_{ij}^t} \right) \\ & + \frac{\partial \xi}{\partial \varepsilon_{ij}^t} \left(\frac{\partial \Psi_T^t}{\partial \bar{\varepsilon}} \frac{\partial \bar{\varepsilon}}{\partial \varepsilon_{kl}^t} + \frac{\partial \Psi_T^t}{\partial J_2^t} \frac{\partial J_2^t}{\partial \varepsilon_{kl}^t} \right) + \frac{\partial^2 \xi}{\partial \varepsilon_{ij}^t \partial \varepsilon_{kl}^t} \Psi_T^t \end{aligned} \tag{B.24}$$

$$H_{ij}^{\theta\sigma} = \xi \left(\frac{\partial^2 \Psi_C^t}{\partial \bar{\varepsilon} \partial s^t} \frac{\partial \bar{\varepsilon}}{\partial \varepsilon_{ij}^t} + \frac{\partial^2 \Psi_C^t}{\partial s^t \partial J_2^t} \frac{\partial J_2^t}{\partial \varepsilon_{ij}^t} \right) + (1-\xi) \left(\frac{\partial^2 \Psi_T^t}{\partial \bar{\varepsilon} \partial s^t} \frac{\partial \bar{\varepsilon}}{\partial \varepsilon_{ij}^t} + \frac{\partial^2 \Psi_T^t}{\partial s^t \partial J_2^t} \frac{\partial J_2^t}{\partial \varepsilon_{ij}^t} \right) + \frac{\partial \xi}{\partial \varepsilon_{ij}^t} \left(\frac{\partial \Psi_C^t}{\partial s^t} - \frac{\partial \Psi_T^t}{\partial s^t} \right) \tag{B.25}$$

$$H^{\theta\theta} = \xi \frac{\partial^2 \Psi_C^t}{\partial s^{t2}} + (1-\xi) \frac{\partial^2 \Psi_T^t}{\partial s^{t2}} + \frac{\partial^2 \Psi_s}{\partial s^{t2}} \tag{B.26}$$

$$H_{ij}^{\sigma\theta} = H_{ij}^{\theta\sigma} \tag{B.27}$$

Appendix C. Consistent tangent

$$\lambda = \sqrt{\frac{\sigma_0^2}{6} \Delta\varepsilon_{ij}^t \Delta\varepsilon_{ij}^t + \frac{\theta_0^2}{4} \Delta s^t \Delta s^t} \tag{C.1}$$

Using Eqs. (B.5), (B.6) and (C.1) and with some algebra:

$$A_{ijkl} d\varepsilon_{kl}^t + B_{ij} ds^t = 2\mu de_{ij} \tag{C.2}$$

$$B_{kl} d\varepsilon_{kl}^t + C ds^t = d\theta \tag{C.3}$$

where

$$A_{ijkl} = \delta_{ik}\delta_{jl} \left(\frac{\sigma_0^2}{3\lambda} + 2\mu \right) + H_{ijkl}^{\sigma\sigma} - \frac{\hat{s}_{ij}\hat{s}_{kl}}{2\lambda} \tag{C.4}$$

$$B_{ij} = H_{ij}^{\sigma\theta} - \frac{\hat{s}_{ij}\hat{\theta}}{2\lambda} \tag{C.5}$$

$$C = \frac{\theta_0^2}{2\lambda} + H^{\theta\theta} - \frac{\hat{\theta}^2}{2\lambda} \tag{C.6}$$

$$\begin{bmatrix} A_{ijkl} & B_{ij} \\ B_{kl} & C \end{bmatrix} \begin{bmatrix} d\varepsilon_{kl}^t \\ ds^t \end{bmatrix} = \begin{bmatrix} 2\mu de_{ij} \\ d\theta \end{bmatrix} \tag{C.7}$$

Inverting Eq. (C.7) leads to:

$$\begin{bmatrix} d\varepsilon_{ij}^t \\ ds^t \end{bmatrix} = \begin{bmatrix} P_{ijkl} & Q_{ij} \\ Q_{kl} & C \end{bmatrix} \begin{bmatrix} 2\mu de_{kl} \\ d\theta \end{bmatrix} \tag{C.8}$$

Now that $d\varepsilon_{ij}^t$ and ds^t are known from Eq. (C.8), the deviatoric stress can be written as:

$$ds_{ij} = 2\mu \left(de_{ij} - d\varepsilon_{ij}^t \right) = 2\mu \left(\delta_{ik}\delta_{jl} - 2\mu P_{ijkl} \right) de_{kl} - 2\mu Q_{ij} d\theta \tag{C.9}$$

where $\mu = E/2/(1+\nu)$ is the shear modulus and $\kappa = E/3/(1-2\nu)$ is the bulk modulus. The incremental stress–strain relationships can now be defined as

$$d\sigma_{ij} = ds_{ij} + \kappa \delta_{ij} de_{kk} - \beta_{ij} d\theta \tag{C.10}$$

References

Abeyaratne, R., Knowles, J.K., 1990. On the driving traction acting on a surface of strain discontinuity in a continuum. J. Mech. Phys. Solids 38 (3), 345–360.

Aleong, D., Dumont, C., Chirani, S.A., Patoor, E., McDowell, D.L., 2002. Transformation surfaces of a textured pseudoelastic polycrystalline cu-Zn-al shape memory alloy. J. Intell. Mater. Syst. Struct. 13, 783–793.

Arghavani, J., Auricchio, F., Naghdabadi, R., Reali, A., Sohrabpour, S., 2010. A 3-D phenomenological constitutive model for shape memory alloys under multiaxial loadings. Int. J. Plast. 26 (7), 976–991.

Auricchio, F., Morganti, S., Reali, A., 2009. Sma numerical modeling versus experimental results. In: ESOMAT 2009-8th European Symposium on Martensitic Transformations. EDP Sciences, p. 08004.

Auricchio, F., Sacco, E., 1997. A one-dimensional model for superelastic shape-memory alloys with different elastic properties between austenite and martensite. Int. J. Non-Linear Mech. 32 (6), 1101–1114.

Ball, J.M., James, R.D., 1989. Fine phase mixtures as minimizers of energy. In: Analysis and Continuum Mechanics. Springer, pp. 647–686.

Berveiller, M., Patoor, E., Buisson, M., 1991. Thermomechanical constitutive equations for shape memory alloys. Le J. Phys. IV 1 (C4), C4–387.

Bhattacharya, K., et al., 2003. Microstructure of Martensite: Why It Forms and how It Gives Rise to the Shape-Memory Effect. Vol. 2, Oxford University Press.
Boyd, J.G., Lagoudas, D.C., 1996. A thermodynamical constitutive model for shape memory materials. Part I. The monolithic shape memory alloy. Int. J. Plast. 12 (6), 805–842.
Brinson, L.C., 1993. One-dimensional constitutive behavior of shape memory alloys: thermomechanical derivation with non-constant material functions and redefined martensite internal variable. J. Intell. Mater. Syst. Struct. 4 (2), 229–242.
Chatziathanasiou, D., Chemisky, Y., Chatzigeorgiou, G., Meraghni, F., 2016. Modeling of coupled phase transformation and reorientation in shape memory alloys under non-proportional thermomechanical loading. Int. J. Plast. 82, 192–224.
Chemisky, Y., Duval, A., Patoor, E., Zineb, T.B., 2011. Constitutive model for shape memory alloys including phase transformation, martensitic reorientation and twins accommodation. Mech. Mater. 43 (7), 361–376.
Christ, D., Reese, S., 2009. A finite element model for shape memory alloys considering thermomechanical couplings at large strains. Int. J. Solids Struct. 46 (20), 3694–3709.
Cisse, C., Zaki, W., Zineb, T.B., 2016. A review of constitutive models and modeling techniques for shape memory alloys. Int. J. Plast. 76, 244–284.
Esomat, 2009. Esomat S3T roundrobin SMA modeling session. http://esomat.fzu.cz/esomat2009/index.php/esomat/esomat2009/modellingsession.
Frost, M., Benesova, B., Sedlak, P., 2016. A microscopically motivated constitutive model for shape memory alloys: Formulation, analysis and computation. Math. Mech. Solids 21 (3), 358–382.
Frost, M., Benesova, B., Seiner, H., Kruzik, M., Sittner, P., Sedlak, P., 2019. Thermomechanical model for niti-based shape mempory alloys covering macroscopic localization of martensitic transformation. Int. J. Solids Struct. 221, 117–129.
Gall, K., Sehitoglu, H., Chumlyakov, Y.I., Kireeva, I., 1999. Tension–compression asymmetry of the stress–strain response in aged single crystal and polycrystalline NiTi. Acta Mater. 47 (4), 1203–1217.
Gillet, Y., Patoor, E., Berveiller, M., 1998. Calculation of pseudoelastic elements using a non-symmetrical thermomechanical transformation criterion and associated rule. J. Intell. Mater. Syst. Struct. 9 (5), 366–378.
Hallai, J.F., Kyriakides, S., 2013. Underlying material response for Lüders-like instabilities. Int. J. Plast. 47, 1–12.
Hartl, D.J., Chatzigeorgiou, G., Lagoudas, D.C., 2010. Three-dimensional modeling and numerical analysis of rate-dependent irrecoverable deformation in shape memory alloys. Int. J. Plast. 26 (10), 1485–1507.
Helm, D., Haupt, P., 2003. Shape memory behaviour: modelling within continuum thermomechanics. Int. J. Solids Struct. 40 (4), 827–849.
Idesman, A., Levitas, V., Preston, D., Cho, J.-Y., 2005. Finite element simulations of martensitic phase transitions and microstructures based on a strain softening model. J. Mech. Phys. Solids 53 (3), 495–523.
Jiang, D., Bechle, N.J., Kyriakides, S., Landis, C.M., 2016. Buckling and recovery of NiTi tubes under axial compression. Int. J. Solids Struct. 80, 52–63.
Jiang, D., Kyriakides, S., Bechle, N.J., Landis, C.M., 2017a. Bending of pseudoelastic NiTi tubes. Int. J. Solids Struct. 124, 192–214.
Jiang, D., Kyriakides, S., Landis, C.M., 2017b. Propagation of phase transformation fronts in pseudoelastic NiTi tubes underuniaxial tension. Extrem. Mech. Lett. 15, 113–121.
Jiang, D., Kyriakides, S., Landis, C.M., Kazinakis, K., 2017c. Modeling of propagation of phase transformation fronts in pseudoelastic NiTi tubes underuniaxial tension. Eur. J. Mech. A Solids 64, 131–142.
Jiang, D., Landis, C.M., 2016. A constitutive model for isothermal pseudoelasticity coupled with plasticity. Shape Memory Superelasticity 2 (4), 360–370.
Lagoudas, D.C., Bo, Z., Qidwai, M.A., 1996. A unified thermodynamic constitutive model for SMA and finite element analysis of active metal matrix composites. Mech. Compos. Mater. Struct. 3 (2), 153–179.
Lagoudas, D.C., Entchev, P.B., Popov, P., Patoor, E., Brinson, L.C., Gao, X., 2006. Shape memory alloys, Part II: Modeling of polycrystals. Mech. Mater. 38 (5–6), 430–462.
Lagoudas, D., Hartl, D., Chemisky, Y., Machado, L., Popov, P., 2012. Constitutive model for the numerical analysis of phase transformation in polycrystalline shape memory alloys. Int. J. Plast. 32, 155–183.
Landis, C.M., 2002. Fully coupled, multi-axial, symmetric constitutive laws for polycrystalline ferroelectric ceramics. J. Mech. Phys. Solids 50 (1), 127–152.
Landis, C., 2003. On the strain saturation conditions for polycrystalline ferroelastic materials. J. Appl. Mech. 70 (4), 470–478.
Levitas, V.I., Ozsoy, I.B., 2009. Micromechanical modeling of stress-induced phase transformations. Part 2. Computational algorithms and examples. Int. J. Plast. 25 (3), 546–583.
Levitas, V.I., Stein, E., 1997. Simple micromechanical model of thermoelastic martensitic transformations. Mech. Res. Commun. 24 (3), 309–318.
Lexcellent, C., Boubakar, M., Bouvet, C., Calloch, S., 2006. About modelling the shape memory alloy behaviour based on the phase transformation surface identification under proportional loading and anisothermal conditions. Int. J. Solids Struct. 43 (3–4), 613–626.
Liang, C., Rogers, C.A., 1997. One-dimensional thermomechanical constitutive relations for shape memory materials. J. Intell. Mater. Syst. Struct. 8 (4), 285–302.
Otsuka, K., Wayman, C.M., 1999. Shape Memory Materials. Cambridge University Press.
Paiva, A., Savi, M.A., Braga, A.M.B., Pacheco, P.M.C.L., 2005. A constitutive model for shape memory alloys considering tensile–compressive asymmetry and plasticity. Int. J. Solids Struct. 42 (11–12), 3439–3457.
Patoor, E., Berveiller, M., 1997. Micromechanical modelling of the thermomechanical behavior of shape memory alloys. In: Mechanics of Solids with Phase Changes. Springer, pp. 121–188.
Patoor, E., Lagoudas, D.C., Entchev, P.B., Brinson, L.C., Xiujie, G., 2006. Shape memory alloys, Part I: General properties and modeling of single crystals. Mech. Mater. 38, 391–429.
Petryk, H., Stupkiewicz, S., 2010. Interfacial energy and dissipation in martensitic phase transformations. Part I: Theory. J. Mech. Phys. Solids 58 (3), 390–408.
Petryk, H., Stupkiewicz, S., Maciejewski, G., 2010. Interfacial energy and dissipation in martensitic phase transformations. Part II: Size effects in pseudoelasticity. J. Mech. Phys. Solids 58 (3), 373–389.
Peultier, B., Zineb, T.B., Patoor, E., 2008. A simplified micromechanical constitutive law adapted to the design of shape memory applications by finite element methods. Mater. Sci. Eng. A 481, 384–388.
Popov, P., Lagoudas, D.C., 2007. A 3-D constitutive model for shape memory alloys incorporating pseudoelasticity and detwinning of self-accommodated martensite. Int. J. Plast. 23 (10–11), 1679–1720.
Qidwai, M., Lagoudas, D., 2000a. Numerical implementation of a shape memory alloy thermomechanical constitutive model using return mapping algorithms. Internat. J. Numer. Methods Engrg. 47 (6), 1123–1168.
Qidwai, M., Lagoudas, D., 2000b. On thermomechanics and transformation surfaces of polycrystalline NiTi shape memory alloy material. Int. J. Plast. 16 (10–11), 1309–1343.
Raniecki, B., Lexcellent, C., 1998. Thermodynamics of isotropic pseudoelasticity in shape memory alloys. Eur. J. Mech. A Solids 17 (2), 185–205.
Savi, M.A., Paiva, A., Baeta-Neves, A.P., Pacheco, P.M., 2002. Phenomenological modeling and numerical simulation of shape memory alloys: a thermo-plastic-phase transformation coupled model. J. Intell. Mater. Syst. Struct. 13 (5), 261–273.
Scalet, G., Niccoli, F., Garion, C., Chiggiato, P., Maletta, C., Auricchio, F., 2019. A three-dimensional phenomenological model for shape memory alloys including two-way shape memory effect and plasticity. Mech. Mater. 136, 103085.
Sedlak, P., Frost, M., Benešová, B., Zineb, T.B., Šittner, P., 2012. Thermomechanical model for NiTi-based shape memory alloys including R-phase and material anisotropy under multi-axial loadings. Int. J. Plast. 39, 132–151.
Tanaka, K., 1986. A thermomechanical sketch of shape memory effect: one-dimensional tensile behavior.
Xu, L., Baxevanis, T., Lagoudas, D.C., 2019. A three-dimensional constitutive model for the martensitic transformation in polycrystalline shape memory alloys under large deformation. Smart Mater. Struct. 28, 074004.
Zhang, M., Baxevanis, T., 2021. An extended three-dimensional finite strain constitutive model for shape memory alloys. J. Appl. Mech. 88, 111010.
Ziolkowski, A., 2007. Three-dimensional phenomenological thermodynamic model of pseudoelasticity of shape memory alloys at finite strains. Contin. Mech. Thermodyn. 19 (6), 379–398.